scientific reports

OPEN

# Spatiotemporal assessment of maize evapotranspiration and surface energy fluxes under varying irrigation regimes using UAV based METRIC

Charan Babu Ankela[1]✉, Neelima T L[1], Chandrasekar K[2], Nidhi Misra[2], Avil Kumar K[1] & Aminullah Noorzai[1,3]✉

**Evapotranspiration (ET) is a key component of the hydrological cycle and is critical for determining crop water requirements. Accurate ET estimation is essential for improving irrigation efficiency, particularly under increasing water scarcity and climate variability. Conventional approaches such as the soil water balance, empirical formulations, the FAO Penman–Monteith method, eddy covariance flux towers, lysimeters, and scintillometers each have limitations related to spatial representativeness, accuracy, or operational cost. Unmanned aerial vehicles (UAVs) equipped with multispectral and thermal sensors offer a high spatial resolution and cost-effective alternative for field-scale assessment of surface energy balance components and ET. In this study, a field experiment was conducted on maize during rabi season of 2022–23 under two irrigation regimes based on depletion of available soil moisture (20% DASM and 40% DASM). UAV-based multispectral (0.05 m) and thermal imagery (0.33 m) were acquired at five crop growth stages and processed using the Mapping Evapotranspiration at High Resolution with Internalized Calibration (METRIC) model to estimate actual evapotranspiration (ETa) and surface energy fluxes. Spatiotemporal analysis showed that the 20% DASM treatment (400 mm) resulted in a 1.7 °C lower land surface temperature, a 16.5% higher NDVI, and an 11% increase in daily ETa compared with the 40% DASM treatment (316 mm), which experienced water stress and a 20% reduction in seasonal ETa. The UAV-based METRIC estimates of daily ETa showed strong agreement with that of Penman-Monteith (PM) combination approach ($R^2 = 0.84$; RMSE = 0.22 mm day$^{-1}$; MAPE = 6.1%), with a slight underestimation of seasonal ETa (–7%). Agreement with the soil water balance method ranged from − 3% to + 3%, demonstrating the capability of the approach to capture irrigation-induced variability in ETa and surface energy fluxes. Overall, the results highlight the potential of UAV-based METRIC for spatiotemporal assessment of crop evapotranspiration and surface energy dynamics to support precision irrigation management.**

**Keywords** Surface energy balance, Crop evapotranspiration, Crop water stress, UAV thermal imagery

Climate change[1] is a significant global concern, exerting immense pressure on various sectors and stands as one of the most formidable challenges of our time[2]. Amid escalating climate change and variation, the global agricultural sector finds itself at a critical crossroads, both a significant contributor to and victim of climate change. The irrigation water management is particularly vulnerable, grappling with hydrological imbalances[3] exacerbated by the rapid depletion of groundwater resources[4,5] and the instability of surface water bodies such as rivers, lakes, and reservoirs. These challenges are indeed compounded by frequent prolonged dry spells and erratic rainfall patterns[6]. Beyond climate change, factors such as population growth, urbanization, global economic development, increasing competition for natural resources, intensive agricultural practices, and fluctuations in trade and food prices exert more immediate impacts on water resources[7]. Collectively, these factors impair both the quantity and quality of water resources[8]. Agriculture sector, consuming around 70% of

[1]Professor Jayashankar Telangana Agricultural University (PJTAU), Hyderabad 500030, Telangana, India. [2]National Remote Sensing Centre (NRSC), ISRO, Balanagar, Hyderabad 500037, Telangana, India. [3]Sayed Jamaluddin Afghani University, Asadabad, Kunar 2801, Afghanistan. ✉email: charanbabu4927@gmail.com; storay2010@gmail.com

available freshwater resources, needs to evaluate existing practices and swiftly adopt efficient water management strategies and modern irrigation technologies to enhance water productivity through optimized water use[9].

In this context, accurate and precise evaluations of crop water needs are thus essential for formulating, implementing, and adopting relevant practices. Evapotranspiration (ET) plays a critical role in this equation, representing largest share of water outflow from agricultural systems, identified as the 'consumptive' fraction of water used by the system, typically crop water requirements[10]. ET is defined as the transfer of water to the atmosphere from the land surface through soil evaporation and plant transpiration. Accurate quantification of ET is vital for optimizing water use and conducting climate change studies[11,12].

Over the years, numerous methods have been devised to estimate ET, each presenting a unique blend of complexity, accuracy, and suitability for specific applications. Among the direct measurement techniques, lysimetry, eddy covariance (EC), Bowen ratio energy balance, and scintillometry stand out, each offering distinct advantages and limitations. Indirect methods, such as the pan evaporation method[13], soil water balance method, FAO Penman-Monteith[13], Hargreaves Samani[14], Blaney and Criddle[15], and Priestly-Taylor[16], represent a range of empirical and reference ET estimation techniques. The application of these methods is frequently constrained by high costs and/or the requirement for extensive surface measurements, which are difficult to obtain over large regions[17]. A common drawback of these techniques is they provide point-based or area-weighted measurements, leading to potential inaccuracies when extrapolated across large, heterogeneous landscapes due to the dynamic nature of energy fluxes[18,19].

Remote sensing technologies can mitigate these limitations by capturing spatial and temporal variations with high precision[17]. In particular, surface energy balance models utilize thermal infrared imagery, to estimate ET. Single-source models, such as the Surface Energy Balance Algorithm for Land (SEBAL)[20] and the Mapping Evapotranspiration at High Resolution with Internalized Calibration (METRIC)[21], conceptualize the land surface as a unified system. In contrast, dual-source models, exemplified by the Two-Source Energy Balance Model (TSEB)[22], distinguish between the energy fluxes from soil and vegetation components.

Numerous studies have validated the effectiveness of various remote sensing models in assessing the spatial and temporal variations of ET using satellite data. For instance, SEBAL has been successfully implemented across multiple regions with notable results in India[23,24], Turkey[25], China[26], and Egypt[27] using Landsat imagery. The METRIC model, an advanced version of SEBAL, has also been widely employed for ET estimation. For example, a study over the Jurala project command area in the Krishna Basin recorded daily ET values ranging from 4 to 10 mm $day^{-1}$ using the METRIC model with Landsat imagery[28].

In Odisha and Saudi Arabia, previous studies reported good agreement with eddy covariance flux tower measurements, albeit with slight overestimations[12,29]. Additionally, METRIC has been successfully implemented using Landsat-7/8 imagery over irrigated agricultural landscapes in Turkey[30–32]. Developed for the continuous estimation of ET over large areas, METRIC is considered one of the most appropriate models for determining the quantity and spatial distribution of ET over crops during the growing season[21,33] as also reported in subsequent studies[34,35].

Nonetheless, achieving field-scale precision remains challenging due to the coarse spatial and temporal resolutions of satellite data, such as Landsat-8/9 (30 m; 8–16 days) and the Moderate Resolution Imaging Spectroradiometer (MODIS; 500 m; 8 days). Given the sensitivity of temperature measurements, high-resolution thermal data is indispensable for accurate estimations of ET. Unmanned Aerial Vehicles (UAVs) emerge as a compelling solution, with researchers increasingly embracing them as cost-effective platforms for scientific data collection. Equipped with advanced high-resolution sensors, UAVs can capture spatial variations at remarkable resolutions, down to the centimeter level, thereby surmounting several limitations inherent in satellite-based methods. They provide flexible flight paths, circumvent cloud cover, operate in favorable weather conditions on demand, and facilitate near real-time data acquisition, rendering them both economically viable and highly efficient.

Recent research has investigated the use of UAVs for ET estimation at high resolutions, building on established energy balance models[36–40]. However, UAV-based ET estimation remains an emerging field that necessitates further validation and exploration[37,40]. Although only a limited number of studies have contributed to this area, they underscore its potential and the need for more extensive research. For instance, data-fusion approaches integrating UAV and Landsat observations have been proposed to improve spatial and temporal ET estimation[41], while a high-resolution METRIC variant (METRIC-HR) has been developed for mixed land-use areas[42]. UAV-based implementation of the METRIC model has also been successfully applied to assess irrigation-induced variability in vineyard systems in Spain[43]. Additionally, other studies have optimized existing models for UAV data to estimate energy fluxes, such as SEBAL[44] and SEBS[45]. Given its demonstrated accuracy and adaptability, the METRIC model is employed in the present study to assess ET under different water regimes in maize (*Zea mays* L.) using UAV-derived spatial data. Maize is the third most important cereal crop in the region, with wide applications in food, feed, fodder, and industrial sectors[46], and Telangana leads the country in maize productivity[47]. In the region, maize is predominantly cultivated under ridge-and-furrow irrigation, where farmers often face challenges related to poor water use efficiency. Both deficit and excess irrigation can adversely affect maize growth, yield, quality, and water productivity[48,49]. Therefore, evaluating existing irrigation practices in relation to crop water requirements is essential for improving sustainable water management.

The present study investigates evapotranspiration anomalies in maize under varying water regimes using UAV-based optical and thermal imagery, implementing the METRIC model with UAV-specific adaptations for high-resolution imagery (hereafter referred to as METRIC-UAV). It is hypothesized that the METRIC-UAV model can effectively capture variations in evapotranspiration of maize under proposed two different irrigation levels.

# Materials and methods

## Study area

A field experiment was conducted at the Maize Research Centre, Agricultural Research Institute, Rajendranagar, Professor Jayashankar Telangana Agricultural University (PJTAU), Hyderabad, India. The maize crop was cultivated in the fetch area of the Eddy Covariance flux tower (EC), positioned at 17° 19' 35" N, 78° 23' 45" E, at an altitude of 541 m above mean sea level (MSL) (Fig. 1). According to Troll's classification, the site falls under the Semi-arid Tropics, with a mean annual rainfall of 919 mm. The region experiences very hot summers and cool winters, receiving 80.4% (738.6 mm) of the mean annual rainfall from the southwest monsoon and 12.2% (113.2 mm) from the northeast monsoon (Fig. 2). During the study period, predominantly westerly to north-westerly winds were prevalent at the study site as shown in the wind rose (Fig. 3). The soil type at the site is clay loam, characterized by a slightly alkaline nature (pH 8.1), medium organic carbon content (0.43%), field capacity of 29% (w/w), permanent wilting point of 12% (w/w), and water-holding capacity of 85 mm. The maize hybrid DHM-117 was sown on November 10, 2022, during the *rabi* season (winter cropping), with a spacing of 60 cm x 20 cm following the standard package of practices recommended by the University. The crop was harvested on March 16, 2023, and March 21, 2023.

## Treatment details

The irrigation treatments employed in the experiment are (1) scheduling irrigation at 20% Depletion of Available Soil Moisture (DASM) (I20) and (2) scheduling irrigation at 40% DASM (I40). Each treatment consists of two plots of 200 m$^2$ (20 m x 10 m) separated from other treatment by 3 m width buffer channels (Fig. 1). Initially two common irrigations, each of 60 mm were provided to both treatments for germination and the establishment of the seedlings. Subsequently, the irrigation was scheduled as per treatment requirements till harvest. Pre calibrated gypsum blocks for the given soil conditions were installed in each plot at 15 & 30 cm depth to monitor soil moisture levels in real time to schedule irrigation as per treatments.

## UAV campaign, sensors, data acquisition and pre-processing

A fixed-wing type UAV, Trinity F90+ (Quantum-Systems Inc., Moorpark, CA, USA), equipped with MicaSense Altum PT sensor (AgEagle Aerial Systems Inc., Kansas, USA), was utilized to capture synchronized multispectral, thermal, and panchromatic data for pixel-aligned outputs (Table 1). Seven UAV flights coinciding with Landsat-8 satellite pass (around 10:00 to 10:30 IST) over the maize fields were carried out, ensuring sufficient (approximately 80%) overlap during each flight throughout the study period. The UAV operated at an average velocity of 17 m s$^{-1}$ at an altitude of 120 m above ground level (AGL). Due to unfavourable weather conditions the UAV flight scheduled for December 10, 2023 was not taken up. The dates of the UAV flights during the cropping season are detailed in the Table 2. Prior to each flight, the Calibrated Reflectance Panel (CRP) was used for radiometric calibration of the optical bands. Every time before the flight, the thermal sensor was stabilized for at least 15 min after resting period[50,51], with automatic non-uniformity correction (NUC) enabled, and its accuracy verified using ground targets (ice, boiling water, bare soil, wet soil) of known surface/skin temperatures measured with soil thermometers and infrared thermometers; empirical line calibration was applied using average measurements. Acquired imageries with different projections and tie points were processed in a photogrammetric software Pix4D (Pix4D S.A., Prilly, Switzerland), where stitching and image correction were carried out followed by orthorectification. The ortho mosaic of multispectral and thermal bands (blue, green, red, red edge, near infrared, thermal bands), Digital Surface Model (DSM), Digital Terrain Model (DTM) were derived as outputs of the preprocessing. The Normalized Difference Vegetation Index (NDVI), Land Surface Temperature (LST) were generated using index calculator and used for further procedure.

$$NDVI = \frac{\mathrm{NIR} - \mathrm{Red}}{\mathrm{NIR} + \mathrm{Red}} \tag{1}$$

$$LST\ (^{o}C) = \frac{\mathrm{LWIR}}{100} - 273.15 \tag{2}$$

## Weather data and ground-based observations

In addition to the spatial data, several ground-based observations during each flight, including meteorological and plant parameters, were recorded and utilized in the study. The meteorological parameters included wind speed (u), air temperature ($T_a$), air pressure (p), and albedo (α), all obtained from various sensors and instruments mounted on the eddy covariance flux tower installed at the site. The field observations like plant height, crop yield and basic irrigation details were recorded manually at regular intervals. Leaf area index was measured by LAI-2200c Plant canopy analyser (LI-COR, Lincoln, NE, USA), and leaf stomatal conductance was measured using porometer and converted to stomatal resistance ($r_L$).

## Methodology

*METRIC-UAV model*

METRIC model, determines latent heat flux as the residual of energy fluxes at the land surface, as described in Eq. (3). Although METRIC was originally developed for Landsat imagery, in the present study it was adapted for high-resolution UAV-based data. The model was implemented step by step using the model builder tool in ArcGIS Pro software (Esri, Redlands, California, USA), with necessary modifications to accommodate the spatial resolution and data structure of UAV imagery. The surface energy balance consists of four primary components: net radiation (Rn), soil heat flux (G), sensible heat flux (H), and latent heat flux (LE or λET). These components are assumed to be in balance at all times, as expressed by the following equation:

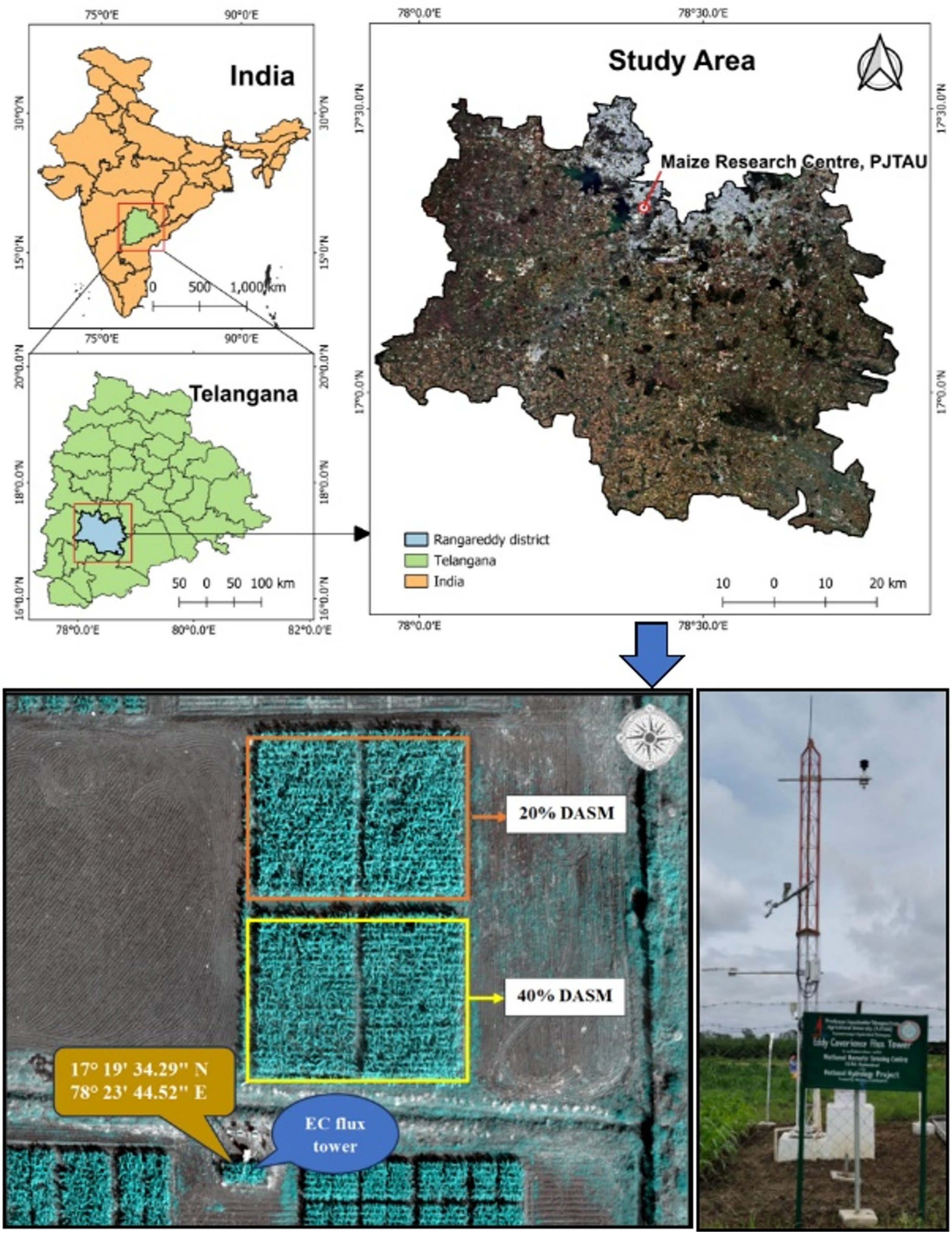


**Fig. 1**. Location and layout of the experimental site. Administrative boundary maps were generated in QGIS 3.40 (QGIS Development Team, Open-Source Geospatial Foundation) using publicly available datasets, and the background satellite image is a Sentinel-2 Level-2A true-colour composite. The lower left panel shows a UAV-derived true-colour orthomosaic of the experimental maize plots, illustrating the 20% and 40% DASM irrigation treatments and the location of the eddy covariance flux tower. UAV imagery was visualized in ArcGIS Pro 3.2 (Esri Inc., Redlands, USA).

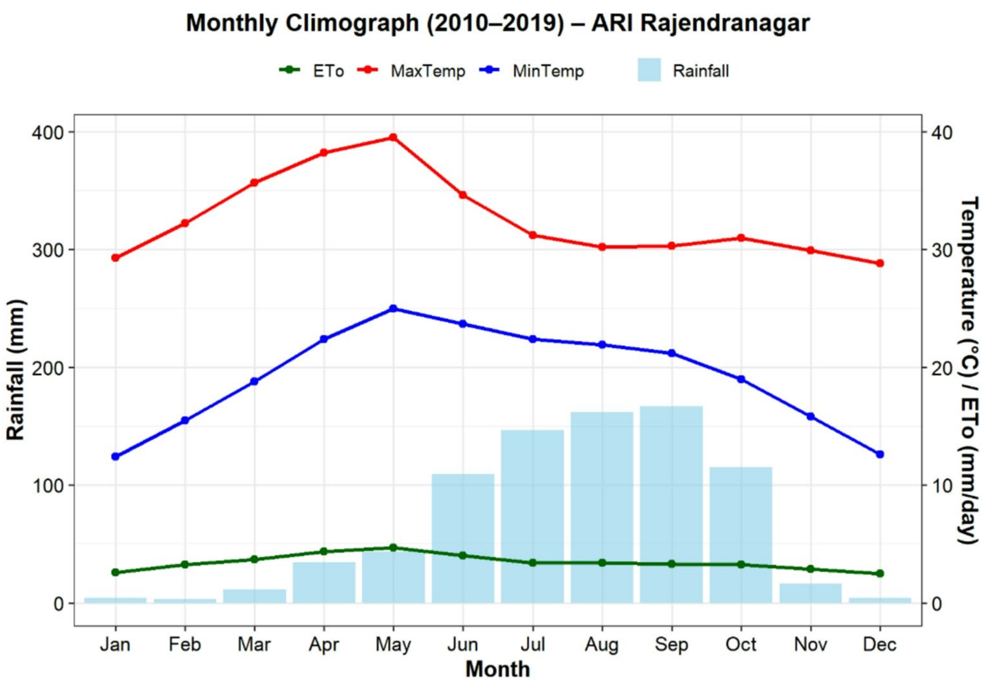


**Fig. 2**. Monthly average rainfall, minimum and maximum air temperature, and reference crop evapotranspiration (ETo) for the period 2010–2019 at the experimental site. Climatic data were obtained from the Agroclimatic Research Centre, PJTAU, Rajendranagar, and the figure was generated using R software (version 4.5.1; https://cran.r-project.org).

$$\lambda ET = Rn - G - H \tag{3}$$

*Where, λET is the latent heat flux, Rn is net radiation, G is soil heat flux, and H is sensible heat flux. All these fluxes are expressed as* W $m^{-2}$ or MJ $m^{-2}$ $day^{-1}$.

Net radiation, the primary driver of surface energy, was determined by estimating all four components of radiation, as expressed in Eq. (4):

$$Rn = (1 - \alpha)Rs + \epsilon_a \sigma T_a^4 - \epsilon_s \sigma T_s^4 \tag{4}$$

*Where, α denotes albedo*; $R_S$ *is insolation or incoming shortwave radiation* (W $m^{-2}$);, σ *is Stefan-Boltzmann's constant* ($5.67 \times 10^8$ W $m^{-2}$ $K^{-4}$); $\varepsilon_a$ and $\varepsilon_s$ *are atmospheric and surface emissivity (dimensionless)*; $T_a$ and $T_s$ *represents air and surface temperatures (K), respectively*.

To solve Eq. (4), a single point value of α, obtained from the EC flux tower, was used due to the unavailability of broadband data required for spatial albedo determination. The same value was applied uniformly to both treatments and directly substituted into the equation. Surface emissivity was estimated using a relationship based on NDVI-derived vegetation proportion[52], following the method described in[53]. Due to the absence of a shortwave infrared (SWIR) band in the UAV data, atmospheric emissivity was estimated from Landsat imagery following the established procedure[54] (Appendix A). However, since both treatment plots fall within a single Landsat pixel, only one atmospheric emissivity value was obtained, regardless of the treatment differences. This single value was then subsequently substituted into Eq. (5).

Soil heat flux was computed using the empirical equation proposed by Bastiaanssen[55] (Eq. 5):

$$G/Rn = \frac{\mathrm{T_s}}{\alpha}[0.0032\alpha + 0.0064\alpha^2][1 - 0.98NDVI^4] \tag{5}$$

*Where* $T_s$ *represents surface temperature (°C).*

When energy flows into the soil, G is positive; conversely, when energy flows out, G is negative.

Sensible heat flux (H), one of the complex components of the energy balance, computed using the aerodynamic equation (similar to Fick's law of diffusion) as a function of temperature difference and resistance to heat transfer (Eq. 6):

$$H = \frac{\rho_{\mathrm{a}} \mathrm{C_p} \Delta \mathrm{T}}{\mathrm{r_{ah}}} \tag{6}$$

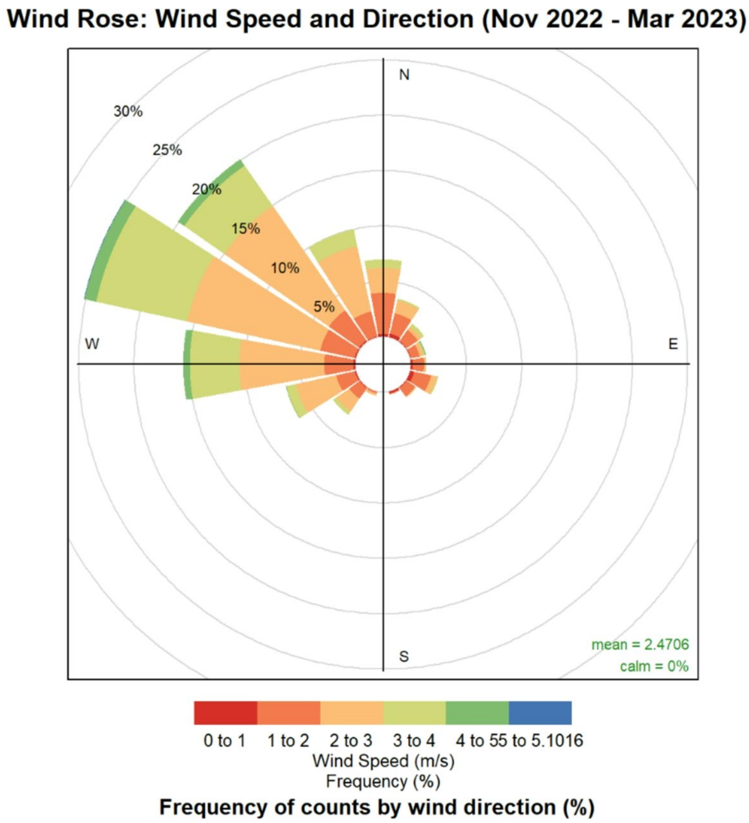


**Fig. 3**. Wind rose showing the frequency distribution of wind speed and wind direction over the study area for the experimental period. Wind data were obtained from the eddy covariance flux tower installed at the experimental site, and the wind rose was generated using R software (version 4.5.1; https://cran.r-project.org).

| Spectral band | | Band width | Resolution (pixels) | GSD at 120 m AGL (cm pixel$^{-1}$) | FOV |
|---|---|---|---|---|---|
| Panchromatic | | - | 4112 × 3008 (12 MP) | 2.49 | 46° x 35° |
| Multi-spectral | Blue (475 mm) | 32 nm | 2064 × 1544 (3.2 MP) | 5.28 | 50° x 38° |
| | Green (560 mm) | 27 nm | | | |
| | Red (668 mm) | 14 nm | | | |
| | Red Edge (717 mm) | 12 nm | | | |
| | NIR (842 mm) | 57 nm | | | |
| Thermal/LWIR (7.5–13.5 µm) (radiometrically calibrated) | | 5 µm | 320 × 256 | 33.5 | 46° x 35° |

**Table 1**. Description of the ALTUM-PT sensor.

| Date | Crop growth stage | UAV flight (Yes/No) | Remarks |
|---|---|---|---|
| November 24, 2022 | Seedling stage (14 DAS) | Yes | - |
| December 10, 2022 | Vegetative phase (30 DAS) | No | Unfavourable weather conditions |
| December 26, 2022 | Vegetative phase (46 DAS) | Yes | - |
| January 11, 2023 | Silking & tasselling (62 DAS) | Yes | - |
| January 27, 2023 | Cob formation (78 DAS) | Yes | - |
| February 12, 2023 | Cob development (94 DAS) | Yes | - |
| February 28, 2023 | Pre maturity (110 DAS) | Yes | - |
| March 16, 2024 | Maturity & harvest (126 DAS) | Yes | - |

**Table 2**. Details of UAV flight schedule during the crop growth season. Note: DAS is days after sowing.

*Where* $\rho_a$ *is air density* (kg m$^{-3}$); $C_p$ *denotes specific heat of air at constant pressure* (1004 J kg$^{-1}$ K$^{-1}$); $r_{ah}$ *is the aerodynamic resistance* (s m$^{-1}$) *between two near-surface heights* $z_1$ and $z_2$ *(typically 0.1 m and 2 m above the zero-plane displacement height, d), and* $\Delta T$ *is the temperature difference (K) between these.*

An iterative approach was adopted to simultaneously solve for ΔT and rah using two anchor pixels (hot and cold), which represent the extremes of ET in the image. Given the limited spatial coverage of UAVs, cold pixel identification is more complex than in satellite-based approaches. UAV imagery covering the entire research station (14.14 ha) was analyzed, where a patch of grass (1–1.5 m height) surrounding the water body was maintained under non-water-stress conditions (Fig. 4). Cold pixels were selected from this grass patch, restricted to the first quartile of the LST histogram and the top 5% of NDVI values, and validated with ground conditions. An ET value of 1.05 ETo was assigned to these pixels. Hot pixels were identified from the last quartile of the LST histogram and the bottom 5% of NDVI values, after excluding outliers and validating with ground conditions—preferably dry, bare soil without irrigation or rainfall in the preceding 10 days, ET is assumed to be zero for hot pixel.

Then, using the energy balance, H was calculated for the selected hot and cold pixels. Subsequently, ΔT and $r_{ah}$ were iteratively determined using Eq. (6), initially assuming neutral atmospheric conditions. The Monin-Obukhov length (L) was then applied to update the air stability conditions accordingly. Based on the linear relationship between surface temperature and ΔT (Eq. 7), pixel-level ΔT and $r_{ah}$ values were updated, and H was calculated for the entire image. The step-wise equations involved in the estimation of sensible heat flux are provided in Appendix B.

$$\Delta T = aTs + b \tag{7}$$

The latent heat flux was calculated by substituting Rn, G, and H in the Eq. (3). This latent heat flux was then converted to instantaneous evapotranspiration ($ET_{inst}$) using the following formula (Eq. 8):

$$ET_{inst} = \frac{\lambda\,\mathrm{ET}}{\lambda}\ \mathrm{X}\ 3600 \tag{8}$$

*where,* $ET_{inst}$ *represents instantaneous ET (mm hr*$^{-1}$*) and 3600 is the conversion factor from seconds to hours.*

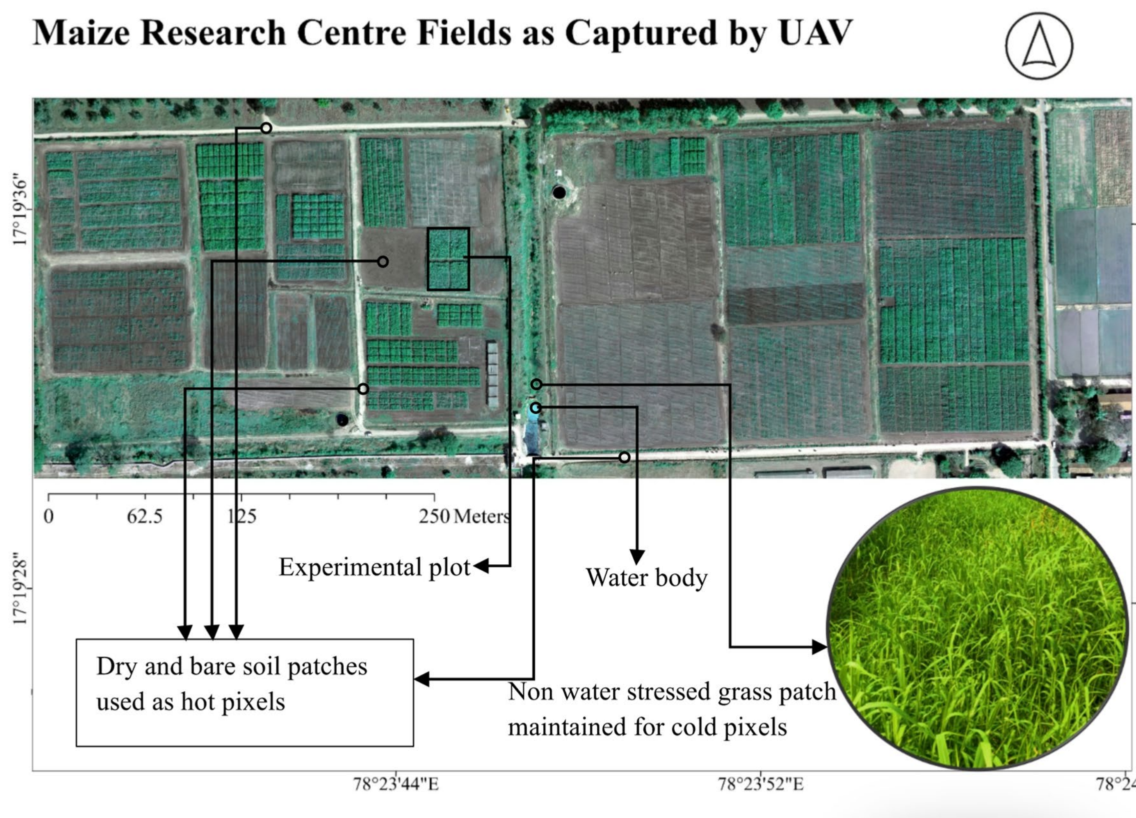


**Fig. 4**. UAV-derived true-colour orthomosaic of the experimental site showing the reference pixels used for internal calibration of the METRIC model. Dry and bare soil patches were selected as hot pixels, while a well-watered grass patch was used as the cold pixel. UAV imagery was processed and visualized in ArcGIS Pro 3.2 (Esri Inc., Redlands, USA).

Further, the reference evapotranspiration fraction ($ET_rF$), which is similar to the crop coefficient (Kc), was calculated as the ratio of instantaneous evapotranspiration to weather-based reference crop evapotranspiration (Eq. 9):

$$ETrF = \frac{\mathrm{ET_{inst}}}{\mathrm{ET_o}} \tag{9}$$

Daily and seasonal ETa were estimated by inverting Eq. (9), expressed as ETa = ETrF × ETr, where ETrF values were interpolated for the intervening days between successive UAV flights and ETr was derived from ground-based weather observations. A detailed workflow, including stepwise equations and procedures, is provided in Appendix B.

*Crop coefficient (Kc)*
As noted earlier, ETrF is analogous to the crop coefficient (Kc). However, Kc curve is constructed using stage-wise average values derived from equation. For this, crop duration is divided into four growth stages—initial (0–20 DAS), crop development (20–55 DAS), mid-season (55–95 DAS), and maturity (95–125 DAS)—as described by Allen et al.[13]. Kc values computed in this study represent actual crop coefficients under irrigation-induced water stress conditions.

$$Kc = \frac{\mathrm{ETa}}{\mathrm{ETo}} \tag{10}$$

*Comparison with Penman Monteith method*
The average daily ETa, seasonal ETa and Kc values derived from the METRIC-UAV model were compared against those obtained using the Penman–Monteith (PM) combination equation. In this study, PM equation refers to the basic Penman Monteith (PM) equation (Chap. 2 in FAO-56 irrigation & drainage paper)[13], which incorporates aerodynamic ($r_a$) and bulk surface resistance ($r_s$) terms. By substituting measured crop biophysical parameters, this equation calculates actual evapotranspiration (ETa) from the maize canopy. It is different from the standard FAO-PM ETo approach that assumes a non-water stressed reference crop (ETc = ETo x Kc).

Meteorological inputs, including air temperature, relative humidity, wind speed, and solar radiation, were obtained from EC flux tower. Only meteorological variables were used; energy balance fluxes (e.g., LE) from the EC flux tower were not used to derive ET. Prior to analysis, the meteorological data were quality-filtered in EddyPro v7.0 (LI-COR Biosciences, USA) using steady-state and developed-turbulence tests, and only data with QC flags 1–4 were retained. To parameterize surface resistance in the PM equation, crop biophysical measurements, such as plant height, leaf area index (LAI), and leaf resistance ($r_L$) were recorded periodically for each irrigation treatment. This data was substituted into Penman Monteith equation to obtain treatment-specific ETa, ensuring consistency in atmospheric forcing while capturing differences in crop response to irrigation.

Although the EC flux tower provides direct ETa measurements through covariance analysis, these represent an integrated flux over its entire footprint, encompassing both irrigation treatments and adjacent land surfaces. Consequently, they do not isolate treatment specific water use. To address this, the Penman-Monteith combination equation was used to calculate ETa at the treatment level. Data from the EC flux tower —specifically energy balance closure and footprint-scale ETa observations—are presented in this study alongside METRIC-UAV derived ETa to illustrate consistency.

Furthermore, seasonal ETa estimates from both the METRIC-UAV approach and the Penman-Monteith method were independently cross validated against estimates obtained using soil water balance (SWB) method. A more detailed explanation of the ET estimation procedures using PM and SWB approaches is available in[56].

## Statistical analysis

The METRIC-UAV derived ETa was validated against ETa estimated using the Penman–Monteith method. Statistical metrics such as the coefficient of determination ($R^2$), root mean square error (RMSE), mean absolute error (MAE), mean absolute percentage error (MAPE), and bias were computed using the following equations (Eqs. 11–15)[57,58].

$$\mathrm{R}^2 = 1 - \frac{\sum_{i=1}^{n}(\mathrm{O_i} - \mathrm{P_i})^2}{\sum_{i=1}^{n}(\mathrm{O_i} - \overline{\mathrm{O}})^2} \tag{11}$$

$$\mathrm{RMSE} = \sqrt{\frac{1}{n}\sum_{i=1}^{n}(\mathrm{P_i} - \mathrm{O_i})^2} \tag{12}$$

$$\mathrm{MAE} = \frac{1}{n}\sum_{i=1}^{n}|\mathrm{P_i} - \mathrm{O_i}| \tag{13}$$

$$\mathrm{MAPE} = \frac{100}{n}\sum_{i=1}^{n}\left|\frac{\mathrm{P_i} - \mathrm{O_i}}{\mathrm{O_i}}\right| \tag{14}$$

$$\mathrm{Bias} = \frac{1}{n}\sum_{i=1}^{n}(\mathrm{P_i} - \mathrm{O_i}) \tag{15}$$

*Where, P is UAV-METRIC estimated ETa (mm day$^{-1}$); $O_i$ is PM derived ETa (mm day$^{-1}$); and $\overline{O}$ is mean of observed values (mm day$^{-1}$) and n is total number of observations.*

## Results and discussion
### Irrigation levels
Two irrigations, totalling approximately 120 mm (60 mm each), were applied uniformly across all treatments—one immediately after sowing to facilitate seedling germination, and another at 12 DAS to ensure proper crop establishment. Subsequently, irrigation was scheduled based on soil moisture depletion, monitored in real time using gypsum blocks, following 20% DASM (I20) and 40% DASM (I40) depletion thresholds. In accordance with the treatment protocols, a total of 400 mm of irrigation water was applied to the I20 plots and 316 mm to the I40 plots, distributed over six and five irrigation events, respectively as detailed in Table 3. Comparable water use by maize under varying irrigation regimes has been reported in the region[59,60] and elsewhere in India[61–63]. In the study region, seasonal water use typically ranges from 300 to 600 mm, depending on soil and weather conditions.

### NDVI and LST
In both treatments, NDVI values progressed from 0.18 during the seedling stage to a peak of 0.75 at the tasselling stage. The initially low NDVI was attributed to sparse vegetation cover and the dominant influence of soil background. As the crop developed, NDVI values increased, peaking at the tasselling stage, and subsequently declined due to senescence (Fig. 5). This trend aligns with the typical NDVI progression reported in previous studies[64–66].

The I20 treatment consistently exhibited higher NDVI values, averaging 16.5% greater than I40 from the knee-high stage onwards (Fig. 5 **&** Fig. 6). This increase was attributed to improved soil moisture availability under the I20 regime, which enhanced vegetation growth. As illustrated in Fig. 6, by the maturity stage (March 16, 2023), the I20 treatment showed a 48.5% higher NDVI than I40, as the latter reached maturity approximately a week earlier, resulting in senesced and fallen vegetation.

Land surface temperature (LST), a critical parameter influencing evapotranspiration, exhibited distinct spatial and temporal dynamics, ranging from 23.8 °C (January 11, 2023) to 34.1 °C (February 12, 2023) (Fig. 7). When averaged over the crop growth period, excluding January 11 and February 12, the I20 plots were 1.7 °C cooler than the I40 plots. These findings are consistent with previous studies. Previous studies have reported a 1.5 °C lower daytime LST in irrigated compared with rainfed maize systems in Nebraska, USA[67], and a 1.15 °C reduction in LST attributable to irrigation effects[68]. Increased soil moisture under the I20 treatment enhanced latent heat flux through the canopy, resulting in a cooling effect and reduced LST. In contrast, moisture deficits under the I40 treatment induced vegetation stress and elevated canopy temperatures, consistent with earlier observations[69]. The temporal pattern revealed nearly identical LST values between treatments during the peak vegetative stage (27 January 2023), in contrast to other growth stages.

Moreover, a negative correlation ($r = -0.66$) was observed between NDVI and LST (Fig. 8), consistent with previously reported inverse relationships between vegetation indices and surface temperature ($r = -0.51$)[70]. Reduced vegetation cover and soil moisture depletion have also been shown to elevate soil surface temperatures, reinforcing the trend observed in this study[71].

### Surface energy fluxes
Balancing energy fluxes is the fundamental principle of this model. Each energy component exhibited distinct variations throughout the crop growth period. For the maize crop, regardless of the treatments, the net radiation

| No. of irrigations | Time of application (DAS) | Discharge (l s$^{-1}$) | Duration of application (min) | Total amount of water applied (mm) |
|---|---|---|---|---|
| 20% DASM | | | | |
| I | 0 | - | - | 60 |
| II | 12 | - | - | 60 |
| III | 26 | 3.31 | 150 | 75 |
| IV | 45 | 3.35 | 135 | 68 |
| V | 79 | 2.90 | 162 | 71 |
| VI | 105 | 2.72 | 165 | 67 |
| Total | | | | 400 |
| 40% DASM | | | | |
| I | 0 | - | - | 60 |
| II | 12 | - | - | 60 |
| III | 36 | 3.29 | 132 | 65 |
| IV | 61 | 2.75 | 173 | 71 |
| V | 90 | 3.32 | 140 | 70 |
| Total | | | | 316 |

**Table 3.** Quantity of irrigation water applied to maize under different irrigation treatments.

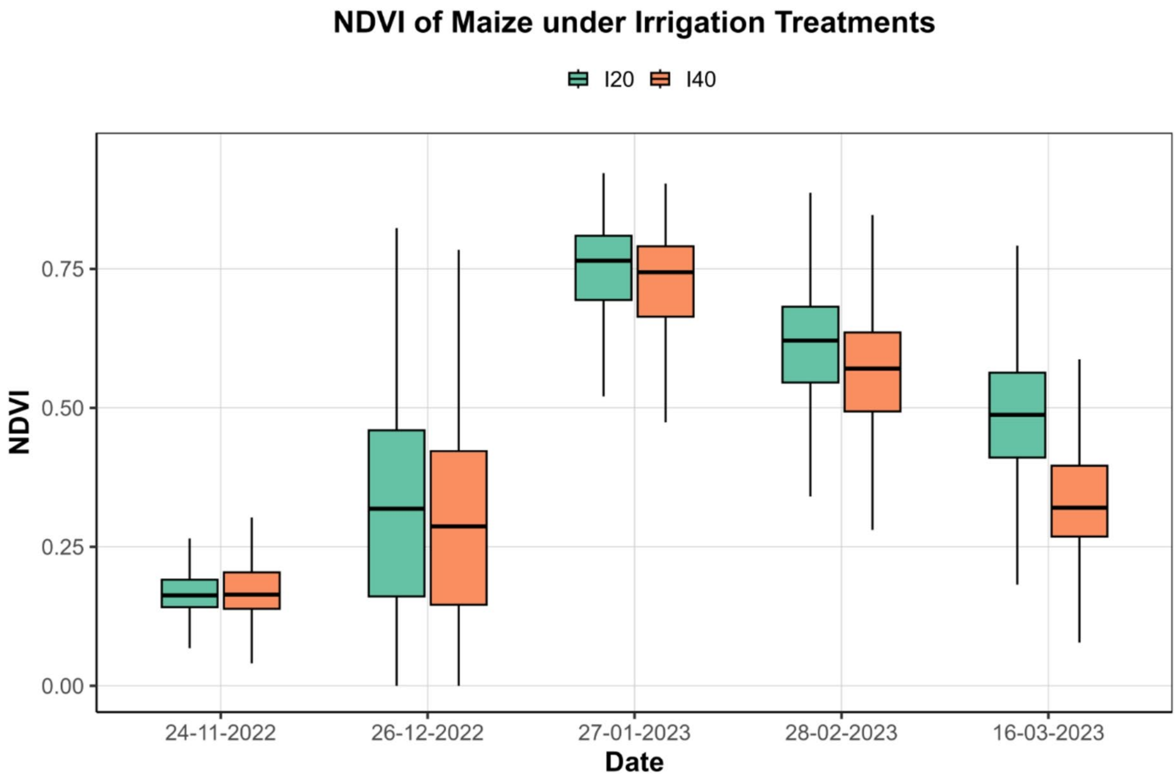


**Fig. 5**. Boxplots showing the distribution of NDVI for maize under the I20 and I40 irrigation treatments on selected UAV acquisition dates during the study period. NDVI was derived from UAV-based multispectral imagery, and the figure was generated using R software (version 4.5.1; https://cran.r-project.org).

ranged from 164.8 W $m^{-2}$ (December 26, 2022) to 453.7 W $m^{-2}$ (January 27, 2023). Soil heat flux ranged from 21.7 W $m^{-2}$ (December 26, 2022) to 46.4 W $m^{-2}$ (February 12, 2023). Latent energy varied from 84.5 W $m^{-2}$ (March 16, 2023) to 173.1 W $m^{-2}$ (December 26, 2022). These observed flux values are consistent with those reported in previous studies[25,28,29,72–75].

*Net radiation (Rn)*

The temporal dynamics of net radiation (Rn) throughout the crop growth period exhibited distinct trends. During the early stages of crop development, when vegetation cover was minimal, Rn values remained relatively low—except on November 24, 2022, when a slightly elevated Rn (266.8 W $m^{-2}$) was observed, due to wet field conditions with exposed soil. As the canopy developed, particularly during January and February, Rn increased markedly, coinciding with higher vegetation cover and leaf area index (LAI) (Appendix C).

Notably, spatial differences in Rn were more pronounced between treatments throughout the crop growth period, with the I20 treatment consistently exhibiting slightly higher Rn values (~ 3%) compared to I40 (Fig. 9). This variation is attributed to relatively denser vegetation and improved soil moisture availability under I20. These observations suggest that both vegetation density and soil moisture positively influence Rn, while dry soil conditions and sparse vegetation—resulting from water stress—negatively affect energy availability. These findings are consistent with previous studies[76].

*Soil heat flux (G)*

During the early part of the season—particularly on November 24 and December 26, 2022—G values were relatively low disregarding the treatments, recorded at 26.6 and 21.7 W $m^{-2}$, respectively. As the canopy developed, G averaged around 31.0 W $m^{-2}$ up to the tasselling stage. Subsequently, from crop maturity to senescence, G gradually increased, ranging between 41.2 and 46.4 W $m^{-2}$. This trend suggests that under dense vegetation, soil heat flux remains low due to shading and reduced solar radiation reaching the soil surface. In contrast, G increased under sparse vegetation conditions where greater solar energy is directly absorbed by the soil. These observations are consistent with previous reports of similar soil heat flux behaviour under variable canopy conditions[77].

Minor spatial variability in G was observed between irrigation treatments (Fig. 10), with the I40 treatment exhibiting approximately 5% higher G than I20. This indicates that deficit moisture conditions can enhance soil heat flux, likely due to reduced evaporative cooling and less canopy cover. When the G/Rn ratio was evaluated, it was found that 7.1% to 12% of net radiation was partitioned into soil heat flux across the crop growth stages. A greater proportion of Rn was allocated to G under dry, bare soil and sparse vegetation conditions, compared

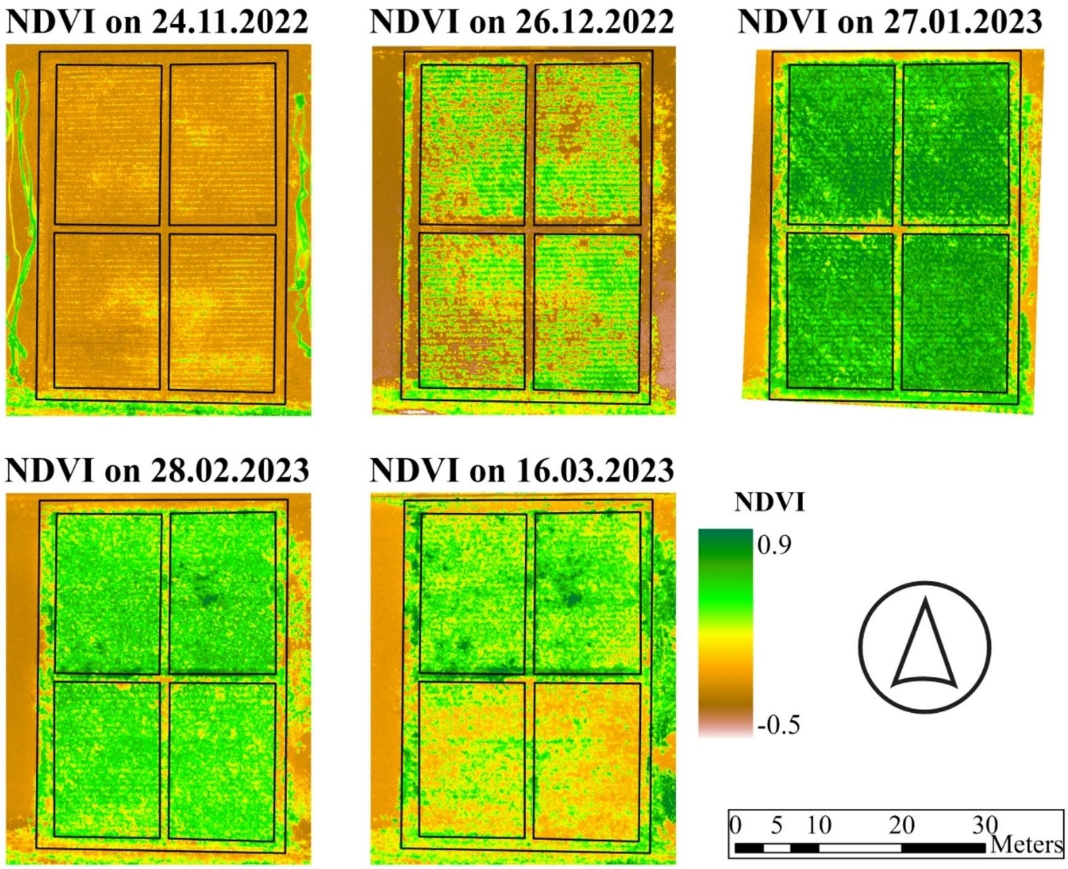


**Fig. 6**. Spatiotemporal variation in NDVI of maize under the I20 and I40 irrigation treatments, derived from UAV-based multispectral imagery for selected flight dates during the maize growing period. Image processing and map visualization were performed using ArcGIS Pro 3.2 (Esri Inc., Redlands, USA).

to full vegetation cover and adequate soil moisture conditions. These findings are consistent with previous observations of similar soil heat flux partitioning in maize under varying irrigation regimes[78].

*Sensible heat flux*
The pattern of sensible heat flux was inversely related to vegetation cover. Lower H values were recorded during periods of peak vegetation, while higher values were observed during the early (seedling) and late (maturity) stages of crop development. Under dry soil moisture conditions, sensible heat flux increased, as evidenced by the I40 treatment exhibiting approximately 5% higher H than I20 (Fig. 11). This trend reflects the reduced partitioning of net radiation into latent heat flux under water stress, resulting in greater energy allocation to sensible heat.

*Latent heat flux (LE)*
In contrast to soil heat flux, latent heat flux exhibited a gradual increase with the development of vegetation cover, reaching its peak when the LAI attained its maximum, followed by a decline during the senescence phase in both irrigation treatments. However, notable spatiotemporal anomalies in LE were observed, influenced by the irrigation regimes (Fig. 12). Specifically, the I20 treatment consistently recorded an average of 16.5% higher LE than I40, indicating that LE is predominantly governed by vegetation dynamics (LAI) and soil moisture availability, which in turn influenced by irrigation management practices. These findings are consistent with previous reports showing approximately 27% higher LE in irrigated maize compared with deficit-irrigated conditions, highlighting the critical role of adequate soil moisture in enhancing evaporative cooling through transpiration[76].

In essence, the observed dynamics of the energy balance components suggest that under conditions of adequate water availability and sufficient soil moisture, LE dominates the energy partitioning, consuming the majority of net radiation. However, as soil moisture declines and water become limiting for evapotranspiration, the available energy is increasingly redirected toward soil heating (G) and sensible heat flux (H), thereby warming the soil and air, respectively. These trends are consistent with previously reported shifts in energy partitioning under variable soil moisture regimes[78]. Moreover, when vegetation indices such as LAI and NDVI are high—indicative of dense, healthy canopies under non-stress conditions—net radiation tends to increase while soil heat flux decreases due to shading, thereby enhancing LE. Conversely, under water-stressed conditions, reduced

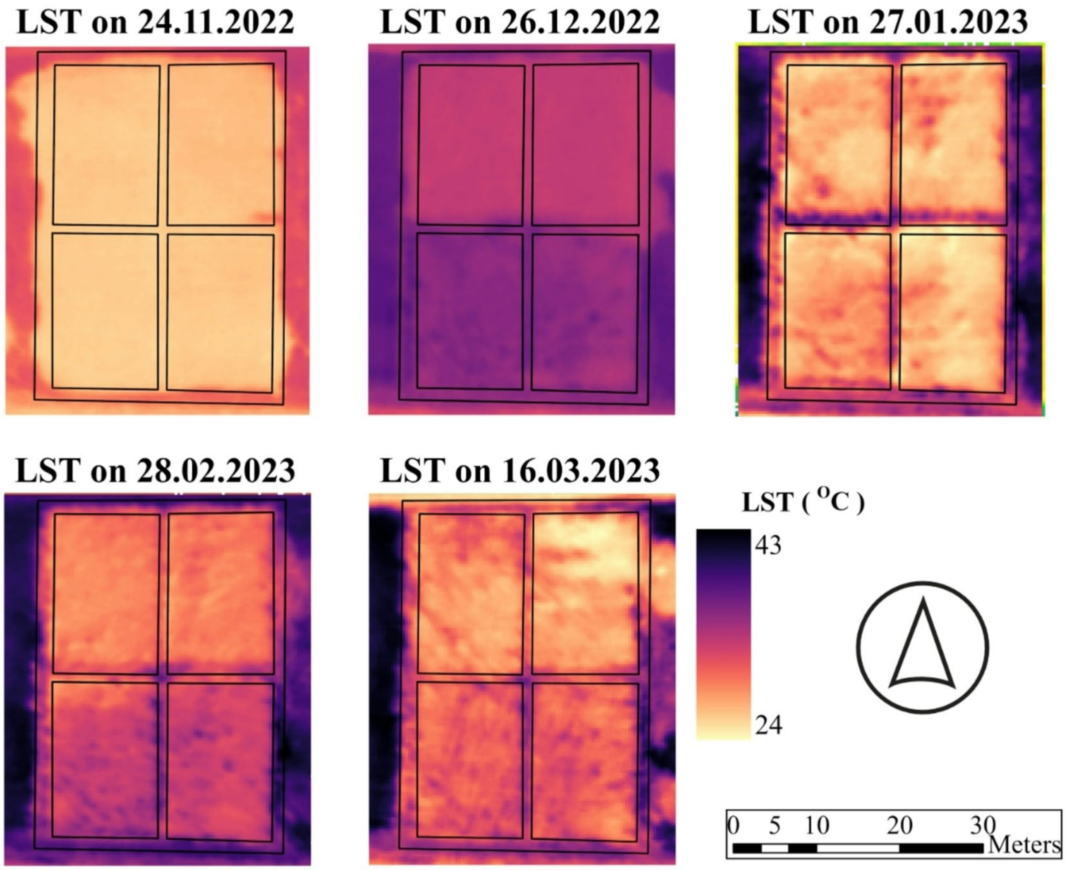


**Fig. 7**. Spatiotemporal variation in LST of maize under the I20 and I40 irrigation treatments derived from UAV-based thermal imagery for selected UAV dates during the maize growing period. Image processing and map visualization were performed in ArcGIS Pro 3.2 (Esri Inc., Redlands, USA).

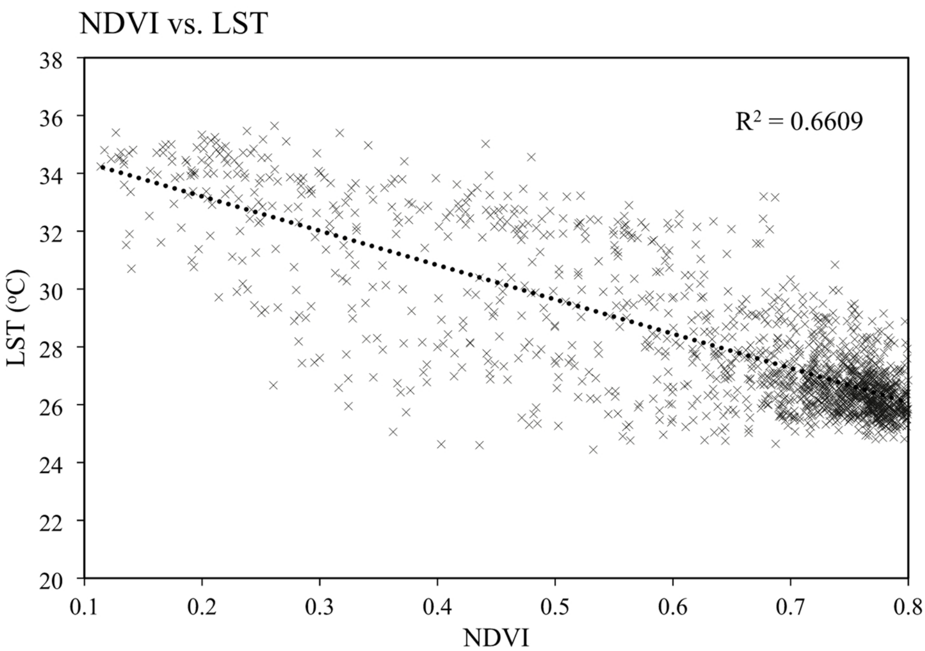


**Fig. 8**. Scatter plot illustrating the relationship between NDVI and LST derived from UAV imagery during the study period. Each point represents pixel-level values, and the dashed line indicates the linear regression fit.

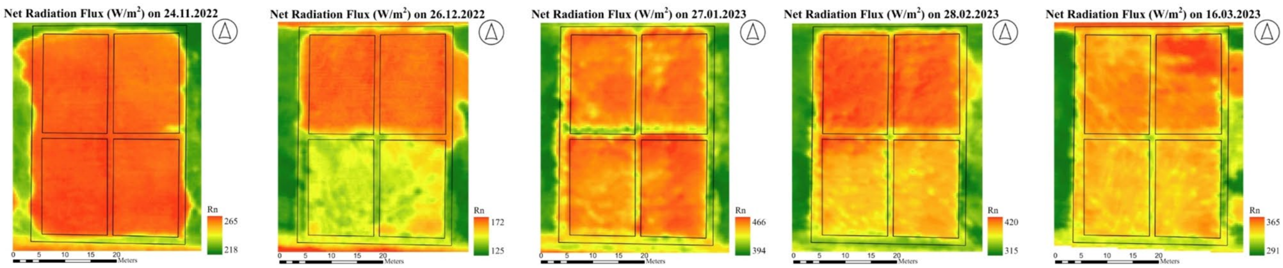


**Fig. 9**. Spatiotemporal variation in net radiation in the maize field under the I20 and I40 irrigation treatments, derived from UAV-based imagery for selected flight dates during the maize growing period. Image processing and map visualization were performed using ArcGIS Pro 3.2 (Esri Inc., Redlands, USA).

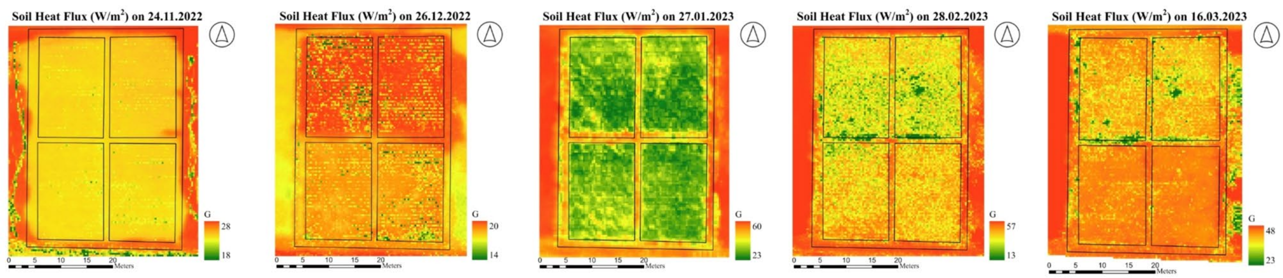


**Fig. 10**. Spatiotemporal variation in soil heat flux in the maize field under the I20 and I40 irrigation treatments, derived from UAV-based imagery for selected flight dates during the maize growing period. Image processing and map visualization were performed using ArcGIS Pro 3.2 (Esri Inc., Redlands, USA).

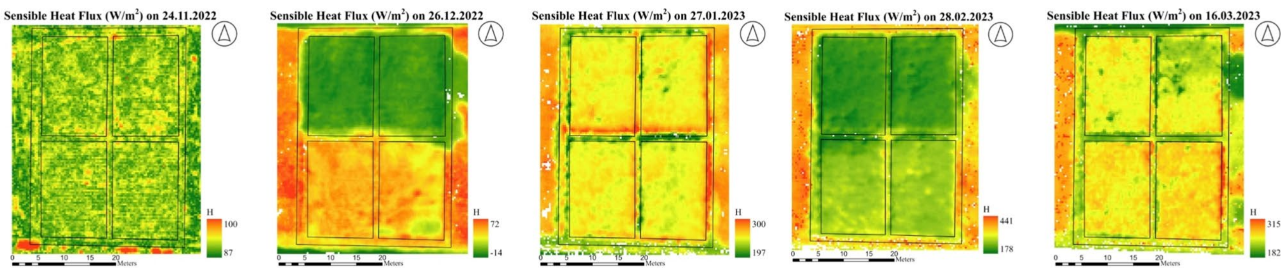


**Fig. 11**. Spatiotemporal variation in sensible heat flux in the maize field under the I20 and I40 irrigation treatments, derived from UAV-based imagery for selected flight dates during the maize growing period. Image processing and map visualization were performed using ArcGIS Pro 3.2 (Esri Inc., Redlands, USA).

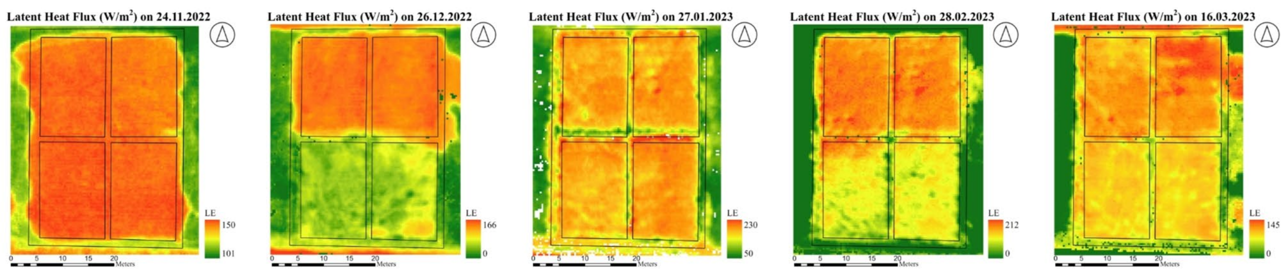


**Fig. 12**. Spatiotemporal variation in latent heat flux in the maize field under the I20 and I40 irrigation treatments, derived from UAV-based imagery for selected flight dates during the maize growing period. Image processing and map visualization were performed using ArcGIS Pro 3.2 (Esri Inc., Redlands, USA).

transpiration leads to a decline in LE, with a corresponding rise in H. Thus, vegetation and soil moisture plays a crucial role in regulating surface energy fluxes.

### 24-hour period evapotranspiration ($ET_{24}$)

For the UAV imagery captured throughout the crop growth period, 24-hour evapotranspiration ($ET_{24}$) was estimated by multiplying the fraction of reference evapotranspiration (ETrF) with corresponding daily reference evapotranspiration (ETo). The $ET_{24}$ values ranged from 1.46 mm day$^{-1}$ (March 16, 2023) to 2.93 mm day$^{-1}$ (January 27, 2023), with an average of 2.28 mm day$^{-1}$ across the dataset (Fig. 13). In general, higher $ET_{24}$ values corresponded to dates when the crop had a well-developed canopy, such as January 27 (2.93 mm day$^{-1}$), February 12 (2.2 mm day$^{-1}$), and February 28 (2.1 mm day$^{-1}$) as shown in Figs. 13 and 14.

Notably, relatively high $ET_{24}$ values were also recorded during the early crop stages—2.2 mm day$^{-1}$ on November 24, 2022, and 2.7 mm day$^{-1}$ on December 26, 2022—despite minimal canopy development. These elevated ET rates are attributed to increased soil evaporation under wet field conditions and limited shading by maize seedlings. Toward the end of the season, during the harvesting stage, $ET_{24}$ declined, with values of 1.85 mm day$^{-1}$ in the I20 treatment and 1.46 mm day$^{-1}$ in the I40 treatment.

Following the imposition of irrigation treatments (post-December 24, 2022), distinct treatment-induced variations in $ET_{24}$ became evident, particularly in imagery acquired on December 26, February 28, and March 16 (Fig. 13). In these instances, the I20 treatment exhibited an average of 20.5%, 60.0%, and 26.7% higher $ET_{24}$, respectively, compared to I40. Notably, $ET_{24}$ values were nearly identical between treatments on January 27, 2023 (I20: 2.93 mm day$^{-1}$; I40: 2.92 mm day$^{-1}$), corresponding to the period of peak vegetation cover and adequate soil moisture in both treatments (Fig. 13).

### Daily evapotranspiration (daily ETa)

Overall, average daily ETa exhibited a progressive increase throughout the crop growth period, with values averaging 2.43 mm day$^{-1}$ and 2.50 mm day$^{-1}$ during the seedling stage under the I20 and I40 treatments, respectively. ETa peaked during the peak vegetative stage at 3.02 mm day$^{-1}$ for I20 and 2.93 mm day$^{-1}$ for I40, before declining to 2.20 mm day$^{-1}$ (I20) and 1.64 mm day$^{-1}$ (I40) as the crop approached physiological maturity (Fig. 14). Comparable trends have been reported in previous studies. For example, lysimeter-based measurements of maize evapotranspiration under Ethiopian conditions showed lower ET during the initial growth stages (2.20

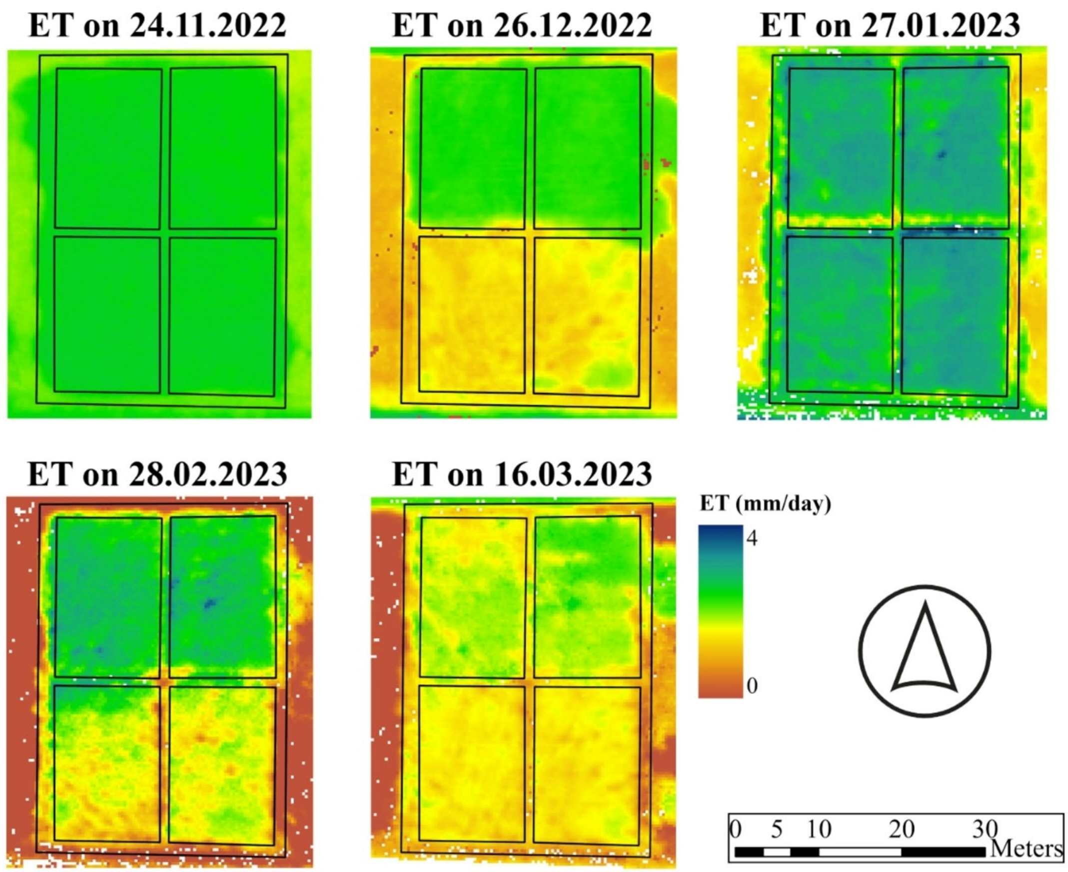


**Fig. 13**. Spatiotemporal variation of 24-h evapotranspiration ($ET_{24}$, mm day$^{-1}$) of maize under the I20 and I40 irrigation treatments derived from UAV-based observations for selected UAV dates during maize growing period. Image processing and map visualization were performed in ArcGIS Pro 3.2 (Esri Inc., Redlands, USA).

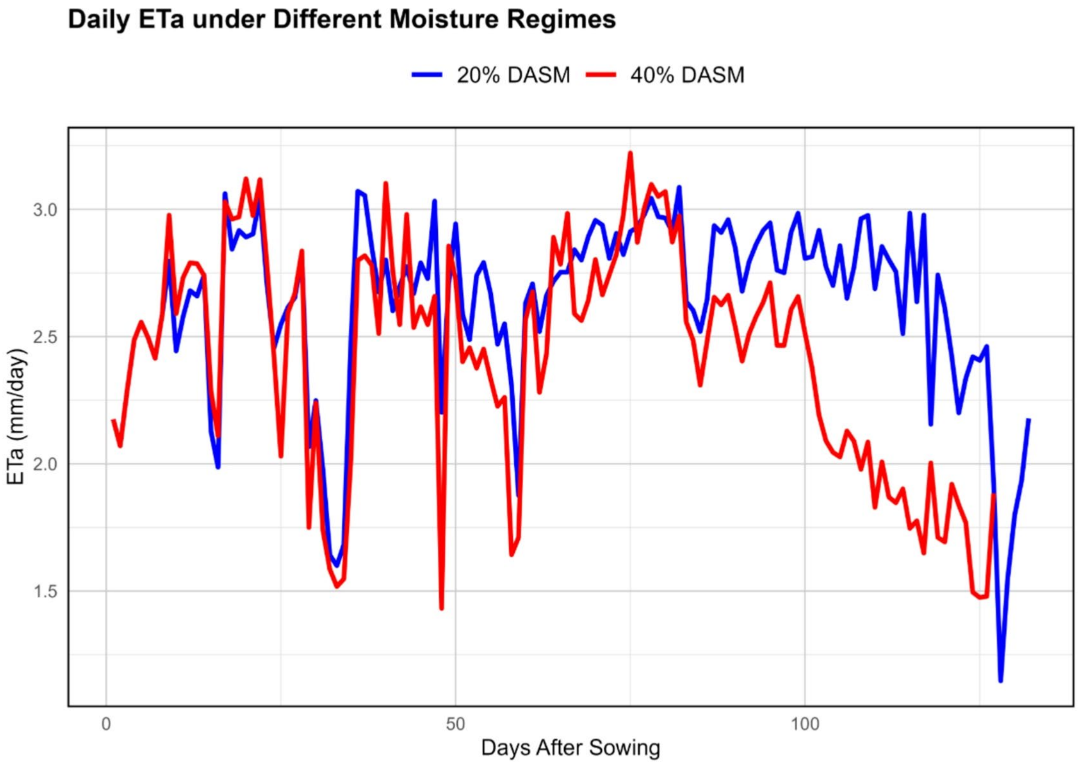


**Fig. 14**. Temporal trends of daily ETa (mm day$^{-1}$) of maize crop under different irrigation treatments, derived using the UAV-based METRIC approach. The time-series plot was generated using R software (version 4.5.1; https://cran.r-project.org).

and 1.82 mm day$^{-1}$) and substantially higher values during midseason (6.83 and 7.20 mm day$^{-1}$ in 2017 and 2018, respectively)[79]. Similarly, other studies have consistently documented a typical ET pattern characterized by initially low values, followed by a midseason peak and a gradual decline toward the end of the growing season. In contrast, the relatively higher ETa observed during the seedling stage in the present study is attributed to increased soil surface evaporation, as the soil remained moist and largely exposed due to sparse canopy cover during early crop establishment.

Prior to the imposition of irrigation treatments, ETa values were nearly identical between the I20 and I40 treatments. However, following the imposition of irrigation treatments at 30 DAS, distinct spatial and temporal anomalies in ETa emerged. The I20 treatment consistently recorded higher ET than I40 (Figs. 13, 14 and 15) due to relatively increased soil moisture availability and plant physiological activity in I20. As a consequence, the maize crop under I40 matured approximately one week earlier than that under I20. The average daily ETa over the entire crop growth period was 2.51 mm day$^{-1}$ for I20 and 2.27 mm day$^{-1}$ for I40, with values ranging from 1.14 to 3.09 mm day$^{-1}$ and 1.34 to 3.15 mm day$^{-1}$, respectively (Fig. 15). Notably, during the maturity and harvest stages (from 100 DAS onwards), the I40 treatment exhibited considerably lower ETa, averaging approximately 0.7 mm day$^{-1}$ less than I20 (Fig. 14), suggesting more pronounced water stress in the later stages under the 40% DASM regime. Conversely, during the peak period of consumptive use (60–70 DAS), ETa values were nearly equal across both treatments, averaging around 2.9 mm day$^{-1}$.

## Seasonal evapotranspiration

Seasonal evapotranspiration is a critical parameter for assessing crop water requirements over the entire crop growth period. In this study, seasonal ETa was estimated by aggregating daily ETa values throughout the crop growth duration for each treatment. The results indicated that the I20 treatment recorded a seasonal ETa of 333 mm, approximately 15% higher than the I40 treatment (288 mm) (Figs. 16 and 17). This difference underscores the effect of irrigation frequency and soil moisture availability on cumulative crop water use. Seasonal evapotranspiration of maize of 351.6 mm, estimated using the pan evaporation method under Hyderabad conditions, has been previously reported[80], with comparable observations documented for Karnal[81].

## Crop coefficient

At the initial stage, Kc values were nearly identical across both treatments, as no irrigation regimes had yet been imposed (Fig. 18). The relatively higher Kc during this stage compared to standard values can be attributed to greater evaporation under exposed wet soil conditions, typical of the seedling stage. For this phase, Kc values may be corrected considering the number of irrigations and ETo following the criteria described in Allen et al.[13].

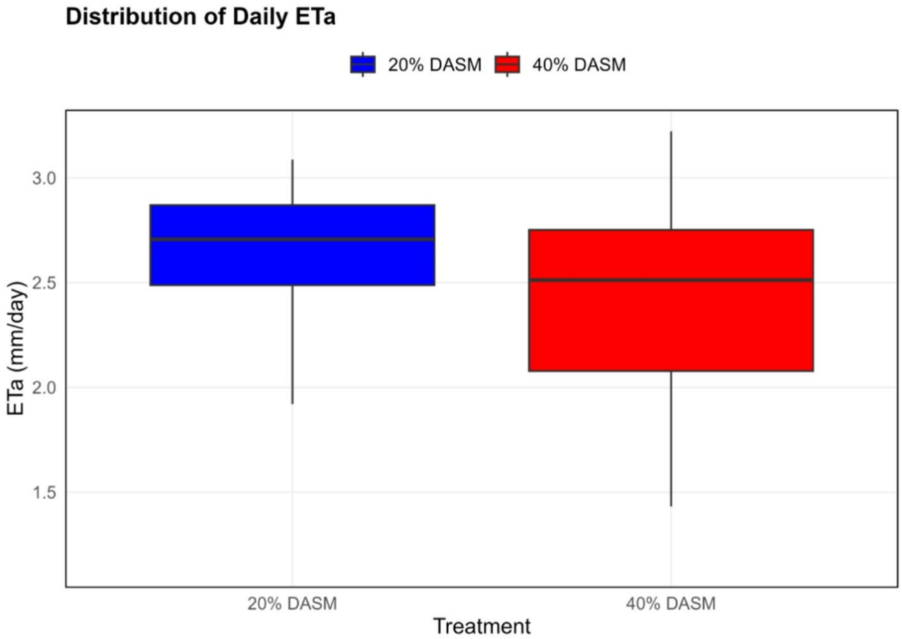


**Fig. 15**. Box plots showing the distribution of daily ETa (mm day$^{-1}$) of maize under the 20% and 40% DASM irrigation treatments estimated using the UAV-based METRIC approach. The statistical visualization was generated using R software (version 4.5.1; https://cran.r-project.org).

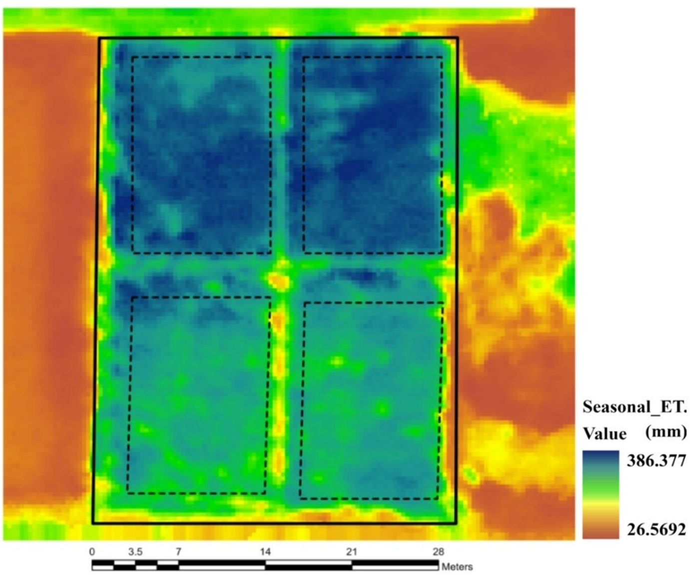


**Fig. 16**. Spatial distribution of seasonal ETa (mm) of maize under 20% and 40% DASM irrigation treatments derived using the UAV-based METRIC approach. Image processing and map visualization were performed in ArcGIS Pro 3.2 (Esri Inc., Redlands, USA).

From the crop development stage onward, Kc remained consistently higher under I20 compared to I40. The divergence was more pronounced during mid-season (1.11 in I20 vs. 1.02 in I40) and maturity (0.60 in I20 vs. 0.40 in I40) (Fig. 18a). Under I40, water stress reduced canopy greenness, as reflected by lower NDVI, accelerating senescence and consequently lowering Kc. In contrast, optimal soil moisture under I20 sustained canopy vigor, resulting in higher Kc values. The Kc values observed under I20 are consistent with previously reported values[60] and align with standard crop coefficient values[13].

The results derived from UAV imagery clearly demonstrate that the two irrigation regimes, I20 and I40, differing by a single irrigation event (60 mm), induced substantial spatiotemporal variations in key crop and energy balance parameters. The I40 treatment resulted in water-deficit conditions, reducing soil moisture

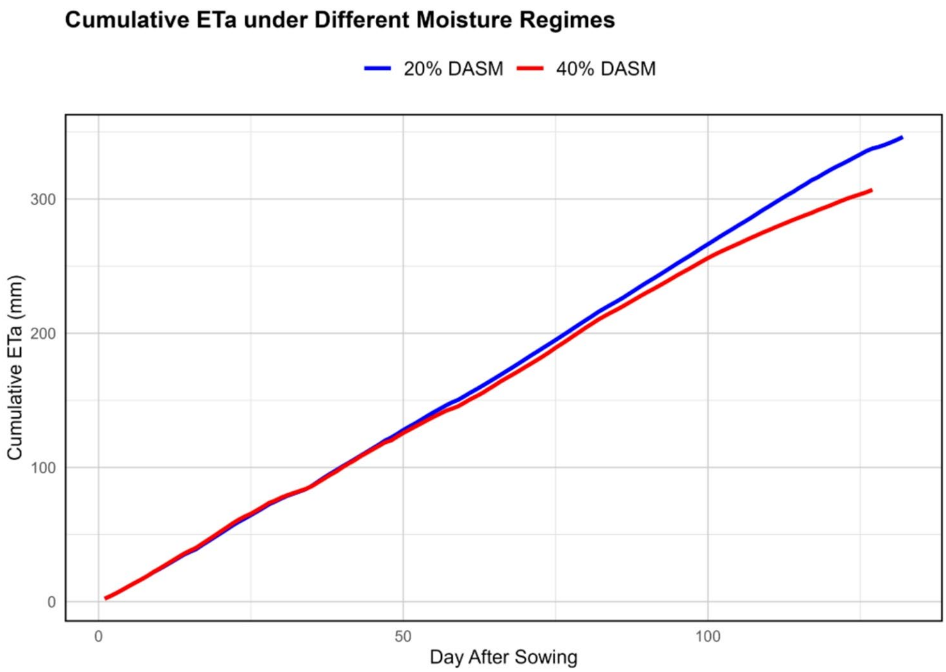


**Fig. 17**. Cumulative ETa (mm) of maize under the 20% and 40% DASM irrigation treatments, derived using the UAV-based METRIC approach. The cumulative ETa time series was generated using R software (version 4.5.1; https://cran.r-project.org).

availability and consequently leading to elevated LST and diminished vegetative development, as reflected by lower NDVI and LAI values. As a result, Rn was reduced, and a larger proportion of the available energy was partitioned into H and G, both of which exhibited higher values under I40 compared to I20. In contrast, the I20 treatment, with greater soil moisture availability, enhanced vegetative growth, evidenced by higher NDVI and LAI values. This dense canopy intercepted greater portion of solar energy, resulting in higher Rn. A substantial portion of this energy was then channelled into LE, supporting higher ET rates.

As a $C_4$ crop, maize likely employed adaptive physiological responses under the water-stressed I40 condition—such as reduced vegetative growth, restricted leaf area, stomatal regulation, and increased surface resistance—to conserve water and maintain cellular turgor, ultimately limiting transpiration losses. Additionally, the diminished soil moisture under I40 also suppressed soil evaporation, thereby contributing to the overall lower ETa observed under this treatment. In contrast, the I20 plots exhibited higher ET due to more favorable moisture conditions that supported both evaporation and transpiration. These differences in water availability and energy partitioning ultimately translated into yield outcomes, with the I20 treatment achieving a higher grain yield of 6.3 t $ha^{-1}$ compared to 5.4 t $ha^{-1}$ under I40.

As previously mentioned, the UAV images captured on January 11 and February 12, 2023, were considered non-representative of typical crop conditions. On both occasions, irrigation had been applied to the I40 treatment just one day prior to the UAV flights—unlike the other image acquisitions, which were conducted without recent irrigation events. As a result, the soil in the I40 plots was at or near saturation to field capacity, with visible surface water. This led to a pronounced reduction in LST by 2.1 °C and 2.2 °C, respectively, compared to the I20 treatment. This contributed to slightly higher Rn and LE, and correspondingly lower G and H in I40 relative to I20. Consequently, the estimated ETa values for these dates were anomalously high for I40 and did not reflect the broader seasonal trends or true treatment effects. Figures showing the spatial variability of those parameters on these dates is given in Appendix D. Given the substantial influence of immediate post-irrigation conditions on soil moisture and surface energy fluxes, these images were excluded from both the daily and seasonal ETa analyses, as they did not accurately represent typical crop and field conditions during those growth stages.

## Comparison of METRIC-UAV with Penman Monteith

*Daily and seasonal ETa*

Daily ETa and seasonal ETa estimated from UAV imagery using the METRIC-UAV approach were compared with ETa computed using the Penman–Monteith method throughout the crop growth period. The comparison of daily ETa revealed a strong correlation, with a high coefficient of determination ($R^2$ = 0.84), low root mean square error (RMSE = 0.22 mm $day^{-1}$), low mean absolute error (MAE = 0.15 mm $day^{-1}$), mean absolute percentage error (MAPE) of 6.1%, and a negative bias of −0.13 mm $day^{-1}$ (Fig. 19). These statistics suggest good agreement between the two methods. However, slight underestimations by METRIC-UAV were observed, particularly at moderate to high ETa levels, as evidenced by data points falling below the 1:1 line (Fig. 19).

At the seasonal scale, METRIC-UAV slightly underestimated cumulative ETa. For I20 and I40 treatments, seasonal ETa was estimated at 333 mm and 288 mm, respectively, compared to 346 mm and 306 mm from

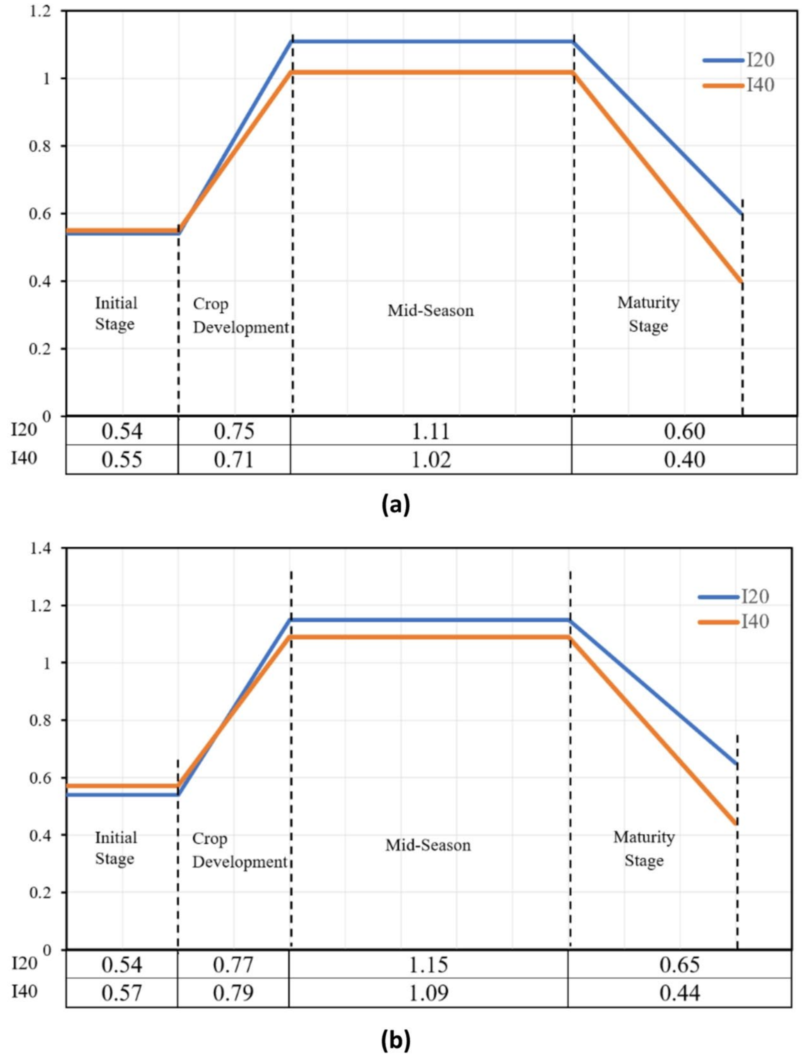


**Fig. 18**. Seasonal variation of crop coefficient (Kc) for maize under the 20% and 40% DASM irrigation treatments derived using (a) the UAV-based METRIC approach and (b) the Penman–Monteith method.

PM, resulting in an average underestimation of ~ 7%. When compared with ET values calculated using the soil water balance (SWB) method (340 mm for I20 and 280 mm for I40), METRIC-UAV slightly overestimated ET under I20 (~ 3%) and slightly underestimated under I40 (~ 3%). When PM method derived ETa values were compared with SWB based ET, it showed 2% and 14% overestimation under I20 and I40 treatments, respectively. Using SWB method the ET difference between the I20 and I40 treatments was 60 mm, but, METRIC UAV and PM showed only 44 mm and 28 mm, respectively. Particularly under water stress (I40) conditions, both the methods (METRIC-UAV & PM) poorly captured (overestimated) the ET compared to SWB method. However, ET anomalies induced by the I20 and I40 water regimes (a difference of single irrigation) relatively small but considerably pronounced.

*Crop coefficient*

Compared with the PM method, the METRIC-UAV model yielded slightly lower Kc values across all growth stages, which was evident from its underestimation of average daily ETa and seasonal ETa (Fig. 18). Notably, the difference between I20 and I40 during mid-season and maturity was more pronounced in METRIC-UAV than in PM as shown in Fig. 18. As discussed earlier, the PM method exhibited comparatively limited sensitivity in capturing ETa anomalies between irrigation regimes, particularly under water-stressed conditions, where it tended to overestimate ET.

## Evaluation against EC flux tower observations

*Energy balance closure consistency*

When the relationship between available energy (Rn - G) and turbulent heat fluxes (LE + H) was evaluated for both METRIC-UAV and EC flux tower data (Fig. 20), METRIC-UAV demonstrated near complete energy balance closure (EBC), whereas EC measurements showed non-closure. METRIC-UAV inherently enforces

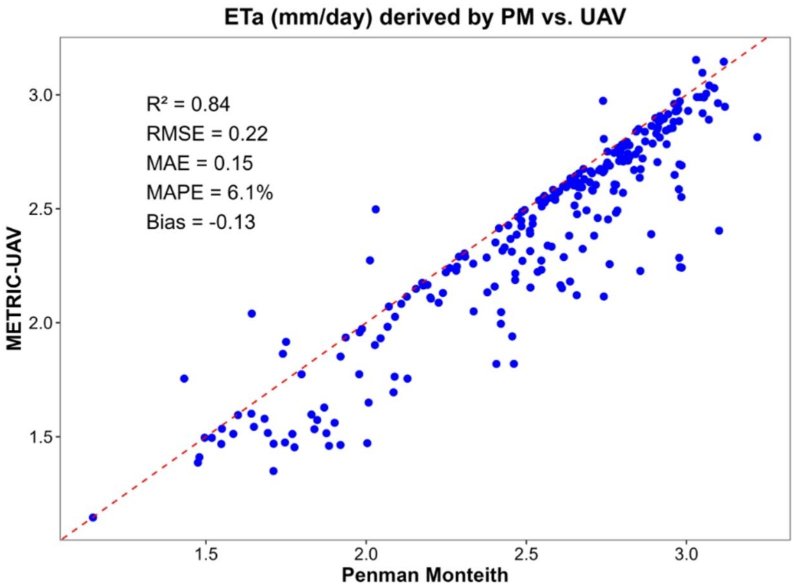


**Fig. 19**. 1:1 Comparison between UAV-based METRIC and Penman–Monteith estimates of ETa (mm day$^{-1}$). The plot was generated using R software (version 4.5.1; https://cran.r-project.org).

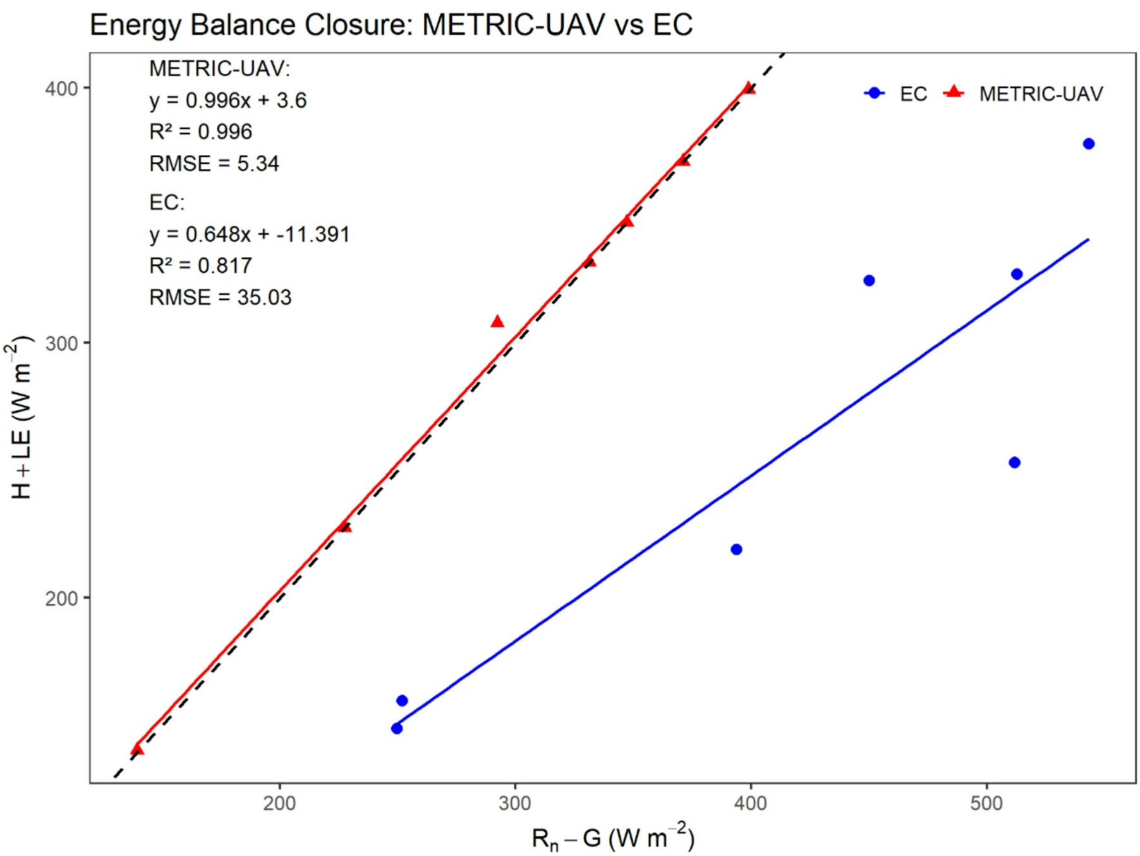


**Fig. 20**. Energy balance closure comparison (available energy vs. turbulent fluxes) between the UAV-based METRIC model and eddy covariance measurements. Solid lines represent linear regressions for each method, while the dashed line is 1:1. The analysis was performed using R software (version 4.5.1; https://cran.r-project.org).

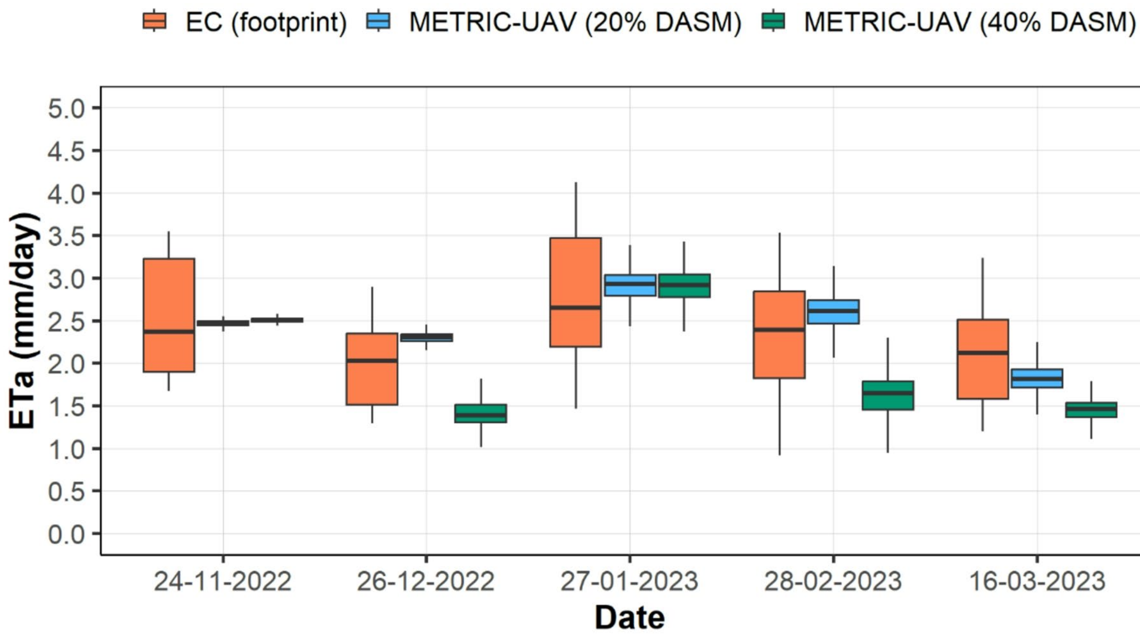


**Fig. 21**. Box plots showing daily ETa (mm $day^{-1}$) of maize during growing period, estimated using the UAV-based METRIC approach for the 20% and 40% DASM irrigation treatments and ETa measured by the EC flux tower footprint for selected UAV dates. The statistical visualization was generated using R software (version 4.5.1; https://cran.r-project.org).

internal energy balance during the calibration of hot and cold pixels, resulting in physically consistent flux partitioning ($R^2 = 0.996$). Minor deviations are attributed to parameterization within the model.

In contrast, the EC flux tower showed incomplete closure ($R^2 = 0.82$), indicating systematic underestimation of turbulent fluxes. Similar imbalance of 15–20% has been reported in several studies[82–84]. Energy non-closure in EC systems may arise from unmeasured storage terms (heat stored in the soil layers above soil heat flux plates and in air column below sensor height), canopy biomass heat storage, sensors alignment, footprint mismatch between available energy and turbulent energy fluxes, and contribution from unmeasured advection and biochemical heat exchange. A detailed explanation of the potential causes is provided in[85]. Despite years of advancement, complete energy balance closure in EC observations remains elusive, and the underlying causes are still not fully understood[86].

Relative to METRIC-UAV, EC fluxes appear lower because EC integrates time averaged fluxes over a heterogenous footprint that includes different land-use types and different crops at different stages. METRIC-UAV, however, represents instantaneous and spatially explicit fluxes directly over the maize canopy within the experimental plots. Due to these real-world biophysical and measurement complexities, this comparison should be interpreted primarily as a diagnostic evaluation of METRIC's internal energy consistency and the degree of agreement with EC-based footprint averages, rather than a strict one-to-one validation.

*Actual evapotranspiration (ETa)*

Although a direct comparison between METRIC-UAV derived ETa and EC-measured ETa is not ideal due to differences in footprint heterogeneity and scale, the ETa estimates obtained on the UAV flight dates are presented in Fig. 21 for interpretation. METRIC captures spatial variability across the field, while EC provides flux measurements overs its source area footprint; therefore, perfect agreement between them is not expected. ETa measured by the EC flux tower, averaged over a ± 60-minute window centered on each UAV overpass time, exhibited larger temporal variability, likely influenced by atmospheric stability, upwind fetch composition, and heterogeneity in the upwind vegetation among other factors. Despite these differences, EC-derived ETa generally remained within or close to the two treatment level METRIC estimates on all flight dates demonstrating the consistency of the METRIC model in representing spatial ET anomalies.

The comparable performance of the METRIC-UAV model can be attributed to several factors, including the high spatial resolution of the imagery and the adequate frequency of image acquisition throughout the crop growth period. However, the observed underestimation may be partly due to the selection of cold pixels. In UAV-based applications, the limited spatial coverage can make it challenging to identify a truly representative cold pixel that meets all the standard conditions. Unlike satellite imagery, which covers a broader spatial extent and thus increases the likelihood of capturing a true cold pixel that defines the upper limit of ET for the scene, UAV imagery may not always contain such a pixel. As a result, there is a strong possibility that a suboptimal cold pixel is selected—one that does not ideally represent the extreme low LST and associated maximum ET. This may lead the model to assume a lower-than-actual maximum ET, contributing to slight underestimation in ETa calculations. This issue of underestimation is not unique to the present study. Similar concerns have been reported in UAV-based applications of the METRIC model. For example, evapotranspiration estimates over almond orchards in Northern California derived using UAV imagery showed good agreement with eddy covariance flux tower measurements ($R^2$ = 0.77), although the UAV-based METRIC approach exhibited notable underestimation, with an RMSE of 1.23 mm day$^{-1}$ and an ETrF mean error of − 0.97 mm day$^{-1}$ when compared with Landsat-based estimates (RMSE = 0.81 mm day$^{-1}$; mean error = − 0.36 mm day$^{-1}$)[41]. Similarly, UAV-based METRIC estimates applied to rice paddies underestimated ET by approximately 7% relative to lysimeter measurements ($r$ = 0.97; RMSE = 0.51 mm day$^{-1}$), while successfully capturing ET anomalies ranging from 0.2% to 8% under varying soil water potential conditions (− 10, − 15 and − 20 kPa relative to 0 kPa)[87].

Furthermore, the METRIC model has been effectively implemented using UAV-based thermal and multispectral imagery to assess evapotranspiration variability in vineyard systems in Spain, capturing distinct responses under different water regimes in crop rows and inter-rows[43]. Similarly, UAV-based METRIC estimates applied to paddy fields under continuous flooding and alternate wetting and drying (AWD) conditions in Peru revealed discernible ET differences and showed good agreement with AquaCrop model simulations ($r$ = 0.783)[88].

Additionally, other alternative models have been explored in the literature for UAV-based ET estimation. Various methods such as the One Source Energy Balance (OSEB), High Resolution Mapping of Evapotranspiration (HRMET), Dual-Temperature-Difference (DTD) model, Two Source Energy Balance (TSEB) model, Machine Learning (ML) algorithms, and SEBAL have also been employed by researchers[89]. Each of these approaches has its own limitations. For instance, the OSEB model tends to underestimate ET, while ML models often require exhaustive datasets[89]. Among these, the TSEB model is widely used, particularly to distinguish surface and canopy ET in complex environments (e.g., orchards and mixed land covers). Several studies have reported promising results. For example, daily and seasonal evapotranspiration estimated using the TSEB model showed strong agreement with the soil water balance method in bell pepper, with $R^2$ values of 0.73 and 0.98, respectively[90]. Similarly, good agreement between TSEB-derived ET and ground-based measurements has been reported in other studies[37,39]. However, application of the TSEB model to UAV data over sorghum fields showed good agreement under fully irrigated conditions ($R^2$ = 0.64) but poor performance under water-deficit conditions, with $R^2$ values ranging from 0.06 to 0.30[91]. Other studies have similarly reported a tendency of the TSEB model to overestimate evapotranspiration under water stress conditions[92,93]. In addition, large discrepancies in H and LE fluxes have been observed when wind speeds exceeded 2.7 m s$^{-1}$[38]. A further challenge with the TSEB model is its sensitivity to errors in the retrieval of absolute LST, which can be particularly problematic with UAV-based sensors and require extensive field measurements. In contrast, METRIC may not require highly accurate LST and large ground-based measurements, making it potentially more robust for UAV applications.

Nonetheless, the evaluation of the METRIC-UAV methodology for ETa estimation within a defined area of interest under varying irrigation levels revealed intricate mapping of key parameters—NDVI, LST, energy fluxes and ET—at exceptionally high spatial resolutions and with reasonably higher accuracy. The detailed mapping at small scales, distinguishing ET variability across row spaces, bunds, crop rows, and even weed patches, was particularly pronounced.

**Challenges and Limitations**.

It is crucial to acknowledge the limitations of this model and consider its practical utility under varying conditions. Several factors can impact the model's effectiveness, particularly in different environmental contexts:

- ***Terrain Variability***: This study was conducted in a flat, agricultural setting. However, applying the model in heterogeneous, sloped, or hilly landscapes may require modifications. These adjustments would need to account for meteorological influences such as surface temperature, solar radiation, and aerodynamic variations that result from changes in altitude.
- ***Pixel Selection***: Limited spatial coverage of UAV imagery makes it particularly challenging to identify a representative cold pixel that meets all standard conditions.
- ***Temporal Representativeness***: Images acquired during or immediately after irrigation or rainfall can substantially alter LST and NDVI (as observed on January 11, 2023, and February 12, 2023), and may not accurately reflect the prevailing crop stage. This poses a particular challenge in ensuring representative conditions, especially during the rainy season.
- ***Solving Atmospheric Emissivity***: In the present study, UAV flights were carefully timed to coincide with Landsat-8 overpasses, enabling accurate estimation of atmospheric emissivity using satellite-derived reference data. However, such alignment is not always feasible in other settings, and in those cases, alternative methods for estimating atmospheric emissivity may be required.

## Conclusions

This study demonstrated the potential of METRIC-UAV in capturing spatial and temporal dynamics of NDVI, LST, surface energy fluxes, and actual evapotranspiration in maize under varying irrigation regimes. Irrigation at 20% DASM with an additional 60 mm event reduced LST by 1.7 °C, increased NDVI by 16.5%, enhanced daily and seasonal ET by 11% and 15%, respectively, and improved grain yield by 14% compared with the water-deficit 40% DASM treatment.

METRIC-UAV provided accurate high-resolution ETa estimates, showing strong agreement with the Penman–Monteith combination method ($R^2$ = 0.84, RMSE = 0.22 mm day$^{-1}$, MAE = 0.15 mm day$^{-1}$, MAPE = 6.1%), and a slight underestimation in seasonal ETa (7%). Deviations from the soil water balance method remained within ± 3%, with minor biases indicating scope for calibration under extreme ET conditions. Overall, METRIC-UAV represents a scalable and adaptable framework for high-resolution ETa monitoring at field scale in agriculture.

Future studies should extend its application to diverse cropping systems and agro-climatic regions, while integrating advanced data-driven approaches to support adaptive, near real-time irrigation management.

## Data availability
The data used in this study are not publicly available due to institutional policy. However, the datasets analysed during the study are available from the corresponding author upon reasonable request.

Received: 22 July 2025; Accepted: 23 December 2025
Published online: 30 January 2026

## References
1. UNFCCC. United Nations Framework Convention on Climate Change. United Nations. (1992). Available at https://unfccc.int/resource/docs/convkp/conveng.pdf
2. Pandve, H. India's National action plan on climate change. *Indian J. Occup. Environ. Med.* **13**, 17. https://doi.org/10.4103/0019-5278.50718 (2009).
3. Singh, V. P., Mishra, A. K., Chowdhary, H. & Khedun, C. P. Climate change and its impact on water resources. In *Modern Water Resources Engineering* 525–569 (Humana, 2014). https://doi.org/10.1007/978-1-62703-595-8_11.
4. Wu, W-Y. et al. Divergent effects of climate change on future groundwater availability in key mid-latitude aquifers. *Nat. Commun.* **11**, 3710. https://doi.org/10.1038/s41467-020-17581-y (2020).
5. Dangar, S., Asoka, A. & Mishra, V. Causes and implications of groundwater depletion in india: a review. *J. Hydrol. (Amst)*. **596**, 126103. https://doi.org/10.1016/j.jhydrol.2021.126103 (2021).
6. Prabhu, S. & Chitale, V. Decoding India's changing monsoon patterns – a tehsil-level assessment. New Delhi: Council on Energy, Environment and Water. Accessed on 19.11–2024 at (2024). https://www.ceew.in/sites/default/files/decoding-how-climate-change-is-changing-monsoon-rainfall-patterns-in-india.pdf
7. Bates, B. C., Kundzewicz, Z., Wu, S. & Palutikof, J. *Climate Change and water. Intergovernmental Panel on Climate Change* (IPCC Secretariat, 2013).
8. FAO. Climate-smart agriculture sourcebook. Food and Agriculture Organization of the United Nations. Accessed on 27.07.2024 at (2013). https://www.fao.org/climate-smart-agriculture-sourcebook/production-resources/module-b6-water/chapter-b6-2/en/
9. Sikka, A. K., Islam, A. & Rao, K. V. Climate-smart land and water management for sustainable agriculture. *Irrig. Drain.* **67**, 72–81. https://doi.org/10.1002/ird.2162 (2018).
10. Brouwer, C. & Heibloem, M. *Irrigation Water Management: Irrigation Water Needs* (Food and Agriculture Organization of the United Nations, 1986).
11. Hoedjes, J. C. B., Chehbouni, A., Jacob, F., Ezzahar, J. & Boulet, G. Deriving daily evapotranspiration from remotely sensed instantaneous evaporative fraction over Olive orchard in semi-arid Morocco. *J. Hydrol. (Amst)*. **354**, 53–64. https://doi.org/10.1016/j.jhydrol.2008.02.016 (2008).
12. Singh, R. P., Paramanik, S., Bhattacharya, B. K. & Behera, M. D. Modelling of evapotranspiration using land surface energy balance and thermal infrared remote sensing. *Trop. Ecol.* **61**, 42–50. https://doi.org/10.1007/s42965-020-00076-8 (2020).
13. Allen, R. G., Pereira, L. S., Raes, D. & Smith, M. *Crop Evapotranspiration Guidelines for Computing Crop Water requirements. FAO Irrigation and Drainage Paper 56* (FAO, 1998).
14. Hargreaves, G. H. & Samani, Z. A. Reference crop evapotranspiration from temperature. *Appl. Eng. Agric.* **1**, 96–99. https://doi.org/10.13031/2013.26773 (1985).
15. Blaney, H. F. & Criddle, W. D. *Determining Consumptive Use and Irrigation Water Requirements* 1275 (US Department of Agriculture, Technical Bulletin No, 1962).
16. Priestley, C. H. B. & Taylor, R. J. On the assessment of surface heat flux and evaporation using large-scale parameters. *Mon Weather Rev.* **100**, 81–92. https://doi.org/10.1175/1520-0493(1972)100%3C0081:OTAOSH%3E2.3.CO;2 (1972).
17. Li, Z. L. et al. A review of current methodologies for regional evapotranspiration Estimation from remotely sensed data. *Sensors* **9**, 3801–3853. https://doi.org/10.3390/s90503801 (2009).
18. Bezerra, B. G., Silva, B. B., Santos, C. A. C. & Bezerra, J. R. C. Actual evapotranspiration Estimation using remote sensing: comparison of SEBAL and SSEB approaches. *Adv. Remote Sens.* **4**, 234–247. https://doi.org/10.4236/ars.2015.43019 (2015).
19. Kamali, M. I. & Nazari, R. Determination of maize water requirement using remote sensing data and SEBAL algorithm. *Agric. Water Manag.* **209**, 197–205. https://doi.org/10.1016/j.agwat.2018.07.035 (2018).
20. Bastiaanssen, W. G. M., Menenti, M., Feddes, R. A. & Holtslag, A. A. M. A remote sensing surface energy balance algorithm for land (SEBAL). 1. Formulation. *J. Hydrol.* **212–213**, 198–212. https://doi.org/10.1016/S0022-1694(98)00253-4 (1998).
21. Allen, R. G., Tasumi, M. & Trezza, R. Satellite-based energy balance for mapping evapotranspiration with internalized calibration (METRIC)—Model. J Irrig Drain Eng 133:380–394. (2007). https://doi.org/10.1061/(ASCE)0733-9437(2007)133:4(380).
22. Norman, J. M., Kustas, W. P. & Humes, K. S. Source approach for estimating soil and vegetation energy fluxes in observations of directional radiometric surface temperature. *Agric. Meteorol.* **77**, 263–293. https://doi.org/10.1016/0168-1923(95)02265-Y (1995).
23. Bala, A., Rawat, K. S., Misra, A. K. & Srivastava, A. Assessment and validation of evapotranspiration using SEBAL algorithm and lysimeter data of IARI agricultural farm, India. *Geocarto Int.* **31**, 739–764. https://doi.org/10.1080/10106049.2015.1076062 (2016).
24. Rawat, K. S., Bala, A., Singh, S. K. & Pal, R. K. Quantification of wheat crop evapotranspiration and mapping: A case study from Bhiwani district of Haryana, India. *Agric. Water Manag.* **187**, 200–209. https://doi.org/10.1016/j.agwat.2017.03.015 (2017).
25. Shamloo, N., Sattari, M. T., Apaydin, H., Kamran, K. V. & Prasad, R. Evapotranspiration Estimation using SEBAL algorithm integrated with remote sensing and experimental methods. *Int. J. Digit. Earth.* **14**, 1638–1658. https://doi.org/10.1080/17538947.2021.1962996 (2021).
26. Zhang, Z., Li, X., Liu, L., Wang, Y. & Li, Y. Influence of mulched drip irrigation on landscape scale evapotranspiration from farmland in an arid area. *Agric. Water Manag.* **230**, 105953. https://doi.org/10.1016/j.agwat.2019.105953 (2020).
27. Fawzy, H. E. D., Sakr, A., El-Enany, M. & Moghazy, H. M. Spatiotemporal assessment of actual evapotranspiration using satellite remote sensing technique in the nile Delta, Egypt. *Alex Eng. J.* **60**, 1421–1432. https://doi.org/10.1016/j.aej.2020.11.001 (2021).
28. Bhargavi, K. P., Mishra, N., Chandrasekar, K., Hakeem, A. & Rao, V. V. Estimation of evapotranspiration using METRIC model. In: 1st International Conference on Sustainable Water Management, 10–11 December 2018, Chandigarh, India. 1(01):262–267 (2018).
29. Madugundu, R. et al. Seasonal dynamics of surface energy fluxes over a center-pivot irrigated cropland in Saudi Arabia. *J. Environ. Biol.* **38**, 743–751. https://doi.org/10.22438/jeb/38/5/MRN-383 (2017).
30. Alsenjar, O., Cetin, M., Aksu, H., Golpinar, M. S. & Akgul, M. A. Actual evapotranspiration Estimation using METRIC model and Landsat satellite images over an irrigated field in the Eastern mediterranean region of Turkey. *Mediterr. Geosci. Rev.* **5**, 35–49. https://doi.org/10.1007/s42990-023-00099-y (2023).
31. Cetin, M., Alsenjar, O., Aksu, H., Golpinar, M. S. & Akgul, M. A. Comparing actual evapotranspiration estimations by METRIC to in-situ water balance measurements over an irrigated field in Turkey. *Hydrol. Sci. J.* **68** (8), 1162–1183. https://doi.org/10.1080/02626667.2023.2198649 (2023).
32. Karahan, H., Cetin, M., Can, M. E. & Alsenjar, O. Developing a new ANN model to estimate daily actual evapotranspiration using limited Climatic data and remote sensing techniques for sustainable water management. *Sustainability* **16** (6), 2481 (2024).
33. Patil, V. C. et al. Assessing agricultural water productivity in desert farming system of Saudi Arabia. *IEEE J. Sel. Top. Appl. Earth Obs Remote Sens.* **8**, 284–297. https://doi.org/10.1109/JSTARS.2014.2320592 (2015).

34. Losgedaragh, Z. S. & Rahimzadegan, M. Evaluation of SEBS, SEBAL, and METRIC models in Estimation of the evaporation from the freshwater lakes (Case study: Amirkabir dam, Iran). *J. Hydrol. (Amst).* **561**, 523–531. https://doi.org/10.1016/j.jhydrol.2018.04.025 (2018).
35. Ali, A. & Al-Mulla, Y. Comparative analysis of two remote sensing models estimating evapotranspiration of As'Suwaiq region. In: 2020 Mediterranean and Middle-East Geoscience and Remote Sensing Symposium (M2GARSS). IEEE, pp 273–276. (2020). https://doi.org/10.1109/M2GARSS47143.2020.9105310
36. Zipper, S. C. & Loheide, I. I. S. P. Using evapotranspiration to assess drought sensitivity on a subfield scale with HRMET, a high-resolution surface energy balance model. *Agric. Meteorol.* **197**, 91–102. https://doi.org/10.1016/j.agrformet.2014.06.009 (2014).
37. Hoffmann, H. et al. Estimating evaporation with thermal UAV data and two-source energy balance models. *Hydrol. Earth Syst. Sci.* **20**, 697–713. https://doi.org/10.5194/hess-20-697-2016 (2016).
38. Ortega-Farías, S. et al. Estimation of energy balance components over a drip-irrigated Olive orchard using thermal and multispectral cameras placed on a helicopter-based unmanned aerial vehicle (UAV). *Remote Sens. (Basel).* **8**, 638. https://doi.org/10.3390/rs8080638 (2016).
39. Xia, T. et al. Mapping evapotranspiration with high-resolution aircraft imagery over vineyards using one- and two-source modelling schemes. *Hydrol. Earth Syst. Sci.* **20**, 1523–1545. https://doi.org/10.5194/hess-20-1523-2016 (2016).
40. Brenner, C., Thiem, C. E., Wizemann, H. D., Bernhardt, M. & Schulz, K. Estimating spatially distributed turbulent heat fluxes from high-resolution thermal imagery acquired with a UAV system. *Int. J. Remote Sens.* **38**, 3003–3026. https://doi.org/10.1080/01431161.2017.1280202 (2017).
41. Mokhtari, A., Ahmadi, A., Daccache, A. & Drechsler, K. Actual evapotranspiration from UAV images: a multi-sensor data fusion approach. *Remote Sens. (Basel).* **13**, 2315. https://doi.org/10.3390/rs13122315 (2021).
42. Elarab, M. The application of unmanned aerial vehicle to precision agriculture: chlorophyll, nitrogen, and evapotranspiration estimation. Dissertation, Utah State University, Logan, Utah. (2016).
43. Ramírez-Cuesta, J. M. et al. Determining grapevine water use under different sustainable agronomic practices using METRIC-UAV surface energy balance model. *Agric. Water Manag.* **281**, 108247. https://doi.org/10.1016/j.agwat.2023.108247 (2023).
44. Montibeller, G. Á. Estimating energy fluxes and evapotranspiration of corn and soybean with an unmanned aircraft system in Ames, Iowa. Master's Thesis, University of Northern Iowa, Cedar Falls, IA, USA. (2017).
45. Wei, J. et al. Mapping super high-resolution evapotranspiration in oasis-desert areas using UAV multi-sensor data. *Agric. Water Manag.* **287**, 108466. https://doi.org/10.1016/j.agwat.2023.108466 (2023).
46. Mishra, P. Maize consumption growth to outpace production in India. The Hindu Business Line, New Delhi (2023). Available at https://www.thehindubusinessline.com/economy/agri-business/maize-consumption-growth-to-outpace-production-in-india/article66755631.ece
47. Government of Telangana. Telangana socio-economic outlook 2023. Planning Department, 1-293. (2023). Available at https://telangana.gov.in/wp-content/uploads/2023/05/Telangana-Socio-Economic-Outlook-2023.pdf
48. Tyagi, N. K., Sharma, D. K. & Luthra, S. K. Determination of evapotranspiration for maize and berseem clover. *Irrig. Sci.* **21**, 173–181. https://doi.org/10.1007/s00271-002-0061-3 (2003).
49. Liu, Y. et al. Maize grain yield and water use efficiency in relation to Climatic factors and plant population in Northern China. *J. Integr. Agric.* **20**, 3156–3169. https://doi.org/10.1016/S2095-3119(20)63428-1 (2021).
50. Kelly, J. et al. Challenges and best practices for deriving temperature data from an uncalibrated UAV thermal infrared camera. *Remote Sens.* **11** (5), 567 (2019).
51. Simpson, J. E. et al. UAS-based high-resolution mapping of evapotranspiration in a mediterranean tree-grass ecosystem. *Agric. For. Meteorol.* **321**, 108981. https://doi.org/10.1016/j.agrformet.2022.108981 (2022).
52. Sekertekin, A. & Bonafoni, S. Land surface temperature retrieval from Landsat 5, 7, and 8 over rural areas: assessment of different retrieval algorithms and emissivity models and toolbox implementation. *Remote Sens.* **12** (2), 294 (2020).
53. Carlson, T. N. & Ripley, D. A. On the relation between NDVI, fractional vegetation cover, and leaf area index. *Remote Sens. Environ.* **62** (3), 241–252 (1997).
54. Allen, R. et al. *METRIC Applications Manual Version 3.0* pp 9–66 (University of Idaho, Kimberly, 2018).
55. Bastiaanssen, W. G. M. Regionalization of surface flux densities and moisture indicators in composite terrain: a remote sensing approach under clear skies in Mediterranean climates. Dissertation, CIP Data Koninklijke Bibliotheek, Den Haag, The Netherlands. (1995). https://doi.org/10.18174/206553
56. Ankela, C. B., Neelima, T. L., Kumar, K. A. & K C Assessment of maize crop evapotranspiration using eddy covariance flux tower weather data. *Int. J. Environ. Clim. Change.* **13**, 2218–2226. https://doi.org/10.9734/ijecc/2023/v13i102884 (2023).
57. Willmott, C. J. & Matsuura, K. Advantages of the mean absolute error (MAE) over the root mean square error (RMSE) in assessing average model performance. *Climate Res.* **30** (1), 79–82. https://doi.org/10.3354/cr030079 (2005).
58. Moriasi, D. N. et al. Model evaluation guidelines for systematic quantification of accuracy in watershed simulations. *Trans. ASABE.* **50** (3), 885–900. https://doi.org/10.13031/2013.23153 (2007).
59. Suneetha, Devi & Rao, P. Water use by corn (*Zea Mays* L.) under limited water supply in sandy loam soil of the Deccan plateau. *J. Res. ANGRAU.* **32** (3), 8–14 (2004).
60. Praveen Rao, V. et al. Drip irrigation of maize: A good agricultural practice for enhanced yield, water saving, and higher profits. *Indian Farming.* **71** (08), 27–32 (2021).
61. Mishra, H., Rathore, T. & Savita, U. Water-use efficiency of irrigated winter maize under cool weather conditions of India. *Irrig. Sci.* **21**, 27–33. https://doi.org/10.1007/s002710100037 (2001).
62. Brar, A. S., Buttar, G. S., Kumar, K. & Vashist Enhancing crop and water productivity of spring maize (Zea mays) through drip fertigation. *Ind. J. Agron.* **64** (1), 87–92 (2019).
63. Kaur, H., Kingra, P., Singh, R., Kaur, S. & Singh, S. Simulation of climate change impact on water productivity of maize in central Punjab. *MAUSAM* **73** (3), 673–682. https://doi.org/10.54302/mausam.v73i3.248 (2022).
64. Tasumi, M., Allen, R. G., Trezza, R. & Wright, J. L. Satellite-based energy balance to assess within-population variance of crop coefficient curves. J Irrig Drain Eng 131:94–109. (2005). https://doi.org/10.1061/(ASCE)0733-9437(2005)131:1(94).
65. Kamble, B., Kilic, A. & Hubbard, K. Estimating crop coefficients using remote sensing-based vegetation index. *Remote Sens. (Basel).* **5**, 1588–1602. https://doi.org/10.3390/rs5041588 (2013).
66. Parmar, S. H., Patel, G. R. & Tiwari, M. K. Assessment of crop water requirement of maize using remote sensing and GIS. *Smart Agricultural Technol.* **4**, 100186. https://doi.org/10.1016/j.atech.2023.100186 (2023).
67. Zhu, P. & Burney, J. Untangling irrigation effects on maize water and heat stress alleviation using satellite data. *Hydrol. Earth Syst. Sci.* **26**, 827–840. https://doi.org/10.5194/hess-26-827-2022 (2022).
68. Yang, Q., Huang, X. & Tang, Q. Irrigation cooling effect on land surface temperature across China based on satellite observations. *Sci. Total Environ.* **705**, 135984. https://doi.org/10.1016/j.scitotenv.2019.135984 (2020).
69. Anderson, M. C., Norman, J. M., Mecikalski, J. R., Otkin, J. A. & Kustas, W. P. A Climatological study of evapotranspiration and moisture stress across the continental united States based on thermal remote sensing: 1. Model formulation. *J. Geophys. Res. Atmos.* **112**, D10117. https://doi.org/10.1029/2006JD007506 (2007).
70. Guha, S. & Govil, H. Land surface temperature and normalized difference vegetation index relationship: a seasonal study on a tropical City. *SN Appl. Sci.* **2**, 1661. https://doi.org/10.1007/s42452-020-03458-8 (2020).
71. El Garouani, M., Amyay, M., Lahrach, A. & Jarar Oulidi, H. Exploring the relationship between LST, LULC, and NDVI in Saïss plain using Geospatial techniques. *E3S Web Conf.* **314**, 04001. https://doi.org/10.1051/e3sconf/202131404001 (2021).

72. Allen, R. G. Using the FAO-56 dual crop coefficient method over an irrigated region as part of an evapotranspiration intercomparison study. *J. Hydrol.* **229**, 27–41. https://doi.org/10.1016/S0022-1694(99)00194-8 (2000).
73. Sett, T. et al. Estimation of instantaneous evapotranspiration using remote sensing-based energy balance technique over parts of North India. *ISPRS Arch. XLII*. **–5**, 345–352. https://doi.org/10.5194/isprs-archives-XLII-5-345-2018 (2018).
74. Wang, X. et al. Energy fluxes and evapotranspiration over irrigated maize field in an arid area with shallow groundwater. *Agric. Water Manag.* **228**, 105922. https://doi.org/10.1016/j.agwat.2019.105922 (2020).
75. Purohit, S. et al. Estimation of evapotranspiration fluxes from Sal (*Shorea robusta* Gaertn.f) forest using METRIC model: case study of Doon Valley, India. *Geocarto Int.* **37**, 5742–5764. https://doi.org/10.1080/10106049.2021.1920630 (2022).
76. Qi, Z. et al. Simulating maize production, water and surface energy balance, canopy temperature, and water stress under full and deficit irrigation. *Trans. ASABE.* **59**, 623–633. https://doi.org/10.13031/trans.59.11067 (2016).
77. Aryalekshmi, B. N., Biradar, R. C., Mohammed Ahamed, J. & Chandrasekar, K. Estimation of evapotranspiration for seasonal water usage analysis. In: 2020 Third International Conference on Advances in Electronics, Computers and Communications (ICAECC). IEEE, pp 1–4. (2020). https://doi.org/10.1109/ICAECC50550.2020.9339527
78. Kar, G. & Kumar, A. Surface energy fluxes and crop water stress index in groundnut under irrigated ecosystem. *Agric. Meteorol.* **146**, 94–106. https://doi.org/10.1016/j.agrformet.2007.05.008 (2007).
79. Negash, T. W., Tefera, A. T. & Bayisa, G. D. Maize (*Zea Mays* L., 1753.) evapotranspiration and crop coefficient in semi-arid region of Ethiopia. *Ital. J. Agrometeorol.* **2**, 55–63. https://doi.org/10.36253/ijam-2777 (2024).
80. Kadasiddappa, M., Praveen Rao, V., Yella Reddy, K. & Tirupataih, K. Yield, water use and water use efficiency of drip irrigated maize in southern Telangana region of AP. In: Proceedings of NGWC, 2013 on problems, challenges and management of GW in agriculture, Coimbatore, Tamil Nadu. 372–376. (2013).
81. Narendra, T. K., Dinesh Sharma, K. & Surendra, L. K. Determination of evapotranspiration for maize and berseem clover. *Irrig. Sci.* **21** (4), 173–181 (2003).
82. Cui, W. & Chui, T. F. M. Temporal and Spatial variations of energy balance closure across FLUXNET research sites. *Agric. Meteorol.* **271**, 12–21. https://doi.org/10.1016/j.agrformet.2019.02.026 (2019).
83. Pastorello, G. et al. The FLUXNET2015 dataset and the oneflux processing pipeline for eddy covariance data. *Sci. Data*. **7**, 225. https://doi.org/10.1038/s41597-020-0534-3 (2020).
84. Mauder, M., Jung, M., Stoy, P., Nelson, J. & Wanner, L. Energy balance closure at FLUXNET sites revisited. *Agric. For. Meteorol.* **358**, 110235. https://doi.org/10.1016/j.agrformet.2024.110235 (2024).
85. Mauder, M., Foken, T. & Cuxart, J. Surface-energy-balance closure over land: a review. *Boundary Layer Meteorol.* **177** (2), 395–426 (2020).
86. Jin, Y., Liu, Y., Liu, J. & Zhang, X. Energy balance closure problem over a tropical seasonal rainforest in Xishuangbanna, Southwest china: role of latent heat flux. *Water* **14** (3), 395. https://doi.org/10.3390/w14030395 (2022).
87. Quille-Mamani, J. A., Ramos-Fernández, L. & Ontiveros-Capurata, R. E. Estimation of rice crop evapotranspiration in Perú based on the METRIC algorithm and UAV images. *Rev. Teledetección.* **58**, 23–38. https://doi.org/10.4995/raet.2021.13699 (2021).
88. Ramos-Fernández, L. et al. Water use efficiency in rice under alternative wetting and drying technique using energy balance model with UAV information and aquacrop in Lambayeque, Peru. *Remote Sens.* **16**, 3882. https://doi.org/10.3390/rs16203882 (2024).
89. Niu, H., Hollenbeck, D., Zhao, T., Wang, D. & Chen, Y. Evapotranspiration Estimation with small UAVs in precision agriculture. *Sensors* **20** (22), 6427. https://doi.org/10.3390/s20226427 (2020).
90. Tunca, E., Köksal, E. S., Torres-Rua, A. F., Kustas, W. P. & Nieto, H. S. Estimation of bell pepper evapotranspiration using two-source energy balance model based on high-resolution thermal and visible imagery from unmanned aerial vehicles. *J. Appl. Rem. Sens.* **16** (2), 022204. https://doi.org/10.1117/1.JRS.16.022204 (2022).
91. Tunca, E. Evaluating the performance of the TSEB model for sorghum evapotranspiration Estimation using time series UAV imagery. *Irrig. Sci.* **42**, 977–994. https://doi.org/10.1007/s00271-023-00887-2 (2023).
92. Morillas, L. et al. Environmental factors affecting the accuracy of surface fluxes from a two-source model in mediterranean drylands: upscaling instantaneous to daytime estimates. *Agric. Meteorol.* **189–190**, 140–158. https://doi.org/10.1016/j.agrformet.2014.01.018 (2014).
93. Bellvert, J. et al. Assimilation of Sentinel-2 biophysical variables into a digital twin for the automated irrigation scheduling of a vineyard. *Water* **15**, 2506. https://doi.org/10.3390/w15142506 (2023).


## Acknowledgements
The authors gratefully acknowledge the resources provided by National Remote Sensing Centre, Hyderabad for this study.

## Author contributions
Data collection, data analysis, data curation, collection of review of literature, original draft preparation, editing - C.B., Ankela & Aminullah, N. Conceptualization, Methodology - Neelima, T.L, Chandrasekar, K. Funding acquisition, Data availabilty, software – Chandrasekar, K., Nidhi Misra, Neelima, T.L. Project administration, Supervision – K Avil Kumar & Chandrasekar, K.

## Funding
This research work was conducted as part of the National Hydrology Project (NHP), implemented by the National Remote Sensing Centre (NRSC), Hyderabad, in collaboration with Professor Jayashankar Telangana Agricultural University (PJTAU), Hyderabad, and funded by the Ministry of Jal Shakti, Government of India.

## Declarations

## Competing interests
The authors declare that they have no known competing financial interests or personal relationships that could have appeared to influence the work reported in this paper.

## Additional information
**Supplementary Information** The online version contains supplementary material available at https://doi.org/10.1038/s41598-025-33916-5.

**Correspondence** and requests for materials should be addressed to C.B.A. or A.N.

**Reprints and permissions information** is available at www.nature.com/reprints.